Earth Syst. Dynam., 15, 1435–1458, 2024
https://doi.org/10.5194/esd-15-1435-2024

Earth System Dynamics
Open Access
EGU

The aerosol pathway is crucial for observationally constraining climate sensitivity and anthropogenic forcing

Ragnhild Bieltvedt Skeie[1], Magne Aldrin[2], Terje K. Berntsen[3], Marit Holden[2], Ragnar Bang Huseby[2], Gunnar Myhre[1], and Trude Storelvmo[3]

[1]CICERO Center for International Climate Research, P.O. Box 1129 Blindern, 0318 Oslo, Norway
[2]Norwegian Computing Center, P.O. Box 114 Blindern, 0314 Oslo, Norway
[3]Department of Geosciences, University of Oslo, P.O. Box 1047 Blindern, 0316 Oslo, Norway

Correspondence: Ragnhild Bieltvedt Skeie (r.b.skeie@cicero.oslo.no)

Received: 2 July 2024 – Discussion started: 9 July 2024
Revised: 19 September 2024 – Accepted: 23 September 2024 – Published: 13 November 2024

Abstract. Climate sensitivity and aerosol forcing are two of the most central, but uncertain, quantities in climate science that are crucial for assessing historical climate as well as future climate projections. Here, we use a Bayesian approach to estimate inferred climate sensitivity and aerosol forcing using observations of temperature and global ocean heat content as well as prior knowledge of effective radiative forcing (ERF) over the industrial period. Due to limited information on uncertainties related to the time evolution of aerosol forcing, we perform a range of sensitivity analyses with idealized aerosol time evolution. The estimates are sensitive to the aerosol forcing pathway, with the mean estimate of inferred effective climate sensitivity ranging from 2.0 to 2.4 K, present-day (2019 relative to 1750) aerosol ERF ranging from -0.7 to $-1.1\,\mathrm{W\,m^{-2}}$, and anthropogenic ERF ranging from 2.6 to $3.1\,\mathrm{W\,m^{-2}}$. Using observations and forcing up to and including 2022, the inferred effective climate sensitivity is 2.2 K with a 1.6 to 3.0 K 90 % uncertainty range. Analysis with more freely evolving aerosol forcing between 1950 and 2014 shows that a strong negative aerosol forcing trend in the latter part of the 20th century is not consistent with observations. Although we test our estimation method with strongly idealized aerosol ERF pathways, our posteriori estimates of the climate sensitivity consistently end up in the weaker end of the range assessed in the Sixth Assessment Report of the Intergovernmental Panel on Climate Change (IPCC AR6). As our method only includes climate feedbacks that have occurred over the historical period, it does not include the pattern effect, i.e., where climate feedbacks are dependent on the pattern of warming which will likely change into the future. Adding the best estimate of the pattern effect from IPCC AR6, our climate sensitivity estimate is almost identical to the IPCC AR6 best estimate and very likely range.

1 Introduction

Historically, anthropogenic aerosols have partly masked the greenhouse-gas-driven warming due to their general cooling effect. The magnitude of this aerosol cooling over the past century is one of the main uncertainties in our understanding of historical climate change (Forster et al., 2021) and a limiting factor for future climate projections (Watson-Parris and Smith, 2022).

Climate feedbacks, especially those governed by highly parameterized processes in climate models (e.g., cloud feedbacks), are another large source of uncertainty in climate predictions (Hawkins and Sutton, 2009) and a reason for the large spread in climate sensitivity in climate models (Zelinka et al., 2020; Sherwood et al., 2020). The total climate feedback strength is commonly quantified by the equilibrium climate sensitivity (ECS), defined as the equilibrium surface air temperature change following a doubling of the atmospheric CO_2 concentration. Complementary to ECS

quantified from climate model simulations, observed historical climate change can be used to constrain the total feedback strength. However, this method is limited by the uncertain historical forcing of the climate (Gregory et al., 2020; Forster, 2016; Knutti et al., 2017), where aerosol forcing is the main source of uncertainty (Forster et al., 2021, 2024). The forcing of the climate system is commonly expressed as effective radiative forcing (ERF), defined as the change in the Earth energy balance relative to pre-industrial conditions due to a change in an external driver of climate change and including adjustments to this forcing that are not mediated by changes in surface temperature (Sherwood et al., 2015). For aerosols, adjustment processes, especially those related to clouds, are important and contribute to the large uncertainties in aerosol ERF (Bellouin et al., 2020). Importantly, both the magnitude of the present-day total aerosol ERF and the historical pathway of aerosol ERF – how aerosols have evolved over time – contribute to the uncertainty in observational constraints on climate sensitivity. Both the climate feedbacks and aerosol ERF are crucial for assessing historical climate change using models (Gillett et al., 2021).

For several models contributing to the sixth phase of the Coupled Model Intercomparison Project (CMIP6), modeled temperatures in the middle to late 20th century are colder than observed (Flynn and Mauritsen, 2020) and show a more rapid warming than in the observations since the early 1980s (Tokarska et al., 2020). Studies point to aerosol ERF that is too strong as part of the reason for the mismatch between modeled and observed temperatures in the second half of the 20th century (Flynn et al., 2023; Flynn and Mauritsen, 2020; Gillett et al., 2021; Smith and Forster, 2021; Zhang et al., 2021). Aerosol ERF is diagnosed from models contributing to CMIP6 within the Radiative Forcing Model Intercomparison Project (Pincus et al., 2016) (RFMIP) and the Aerosol Chemistry Model Intercomparison Project (Collins et al., 2017) (AerChemMIP). It is noteworthy that the aerosol ERF time evolutions from these models, driven by the same emission inventory, show considerable variation, with the timing of the peak in negative total aerosol ERF varying from 1975 to 2010 (C. J. Smith et al., 2021).

Estimated climate sensitivity based on historical observations has also been found to be sensitive to different aerosol forcing pathways (Skeie et al., 2018). In IPCC AR6, time series of ERF from 1750 to 2019 were presented for a range of climate forcers (Forster et al., 2021), and more recently these have been extended to 2022 (Forster et al., 2023) and 2023 (Forster et al., 2024). The uncertainties in these forcing time series are presented as the 5th and 95th percentiles, but uncertainties in the time evolution of these forcings are not quantified. As shown in C. J. Smith et al. (2021), the different representations of model physics result in different pathways of the total aerosol ERF. In addition, uncertainties in aerosol and aerosol precursor emissions will add additional uncertainties to the aerosol time evolution (C. J. Smith et al., 2021).

In the emission inventory provided for CMIP6 there are no quantifications of uncertainties (Hoesly et al., 2018). For historical global anthropogenic SO_2 emissions, uncertainties of 8 %–14 % (5 % to 95 % confidence interval) have previously been estimated, while regional emission uncertainties are larger (Smith et al., 2011). For black and organic carbon emissions from fuel combustion, uncertainties in global emissions are larger than a factor of 2 (Bond et al., 2007). The lifetime of aerosols is short, on the order of days (Samset et al., 2014; Textor et al., 2007) and both chemical conversion in the atmosphere (Manktelow et al., 2007) and the forcing efficiency (Shindell et al., 2015; Kasoar et al., 2018) are dependent on the location of emissions. Therefore, uncertainties in geographical distribution and their trends, as well as the total quantity of emissions, will add additional uncertainties to aerosol ERF as diagnosed in the models.

Due to air pollution quality controls, the global emissions of SO_2 have been rapidly decreasing due to emission controls in Europe and North America (Hoesly et al., 2018; Aas et al., 2019) and over the latest decade in East Asia (Zheng et al., 2018). From both observations and modeling efforts, there is now robust evidence of a reversal of the trend in aerosol ERF, with a reduced cooling contribution from aerosols over the last decades (Quaas et al., 2022).

Here, building on previous work (Skeie et al., 2018, 2014; Aldrin et al., 2012), we investigate the importance of aerosol ERF time evolution for observational constraints on ERF and climate sensitivity. The estimated climate sensitivity is the inferred effective climate sensitivity (ECS_{inf}), and for known reasons ECS_{inf} differs from ECS as calculated in climate models (e.g., Armour et al., 2024; Sherwood et al., 2020), which we will discuss in the Discussion section. We use a Bayesian framework considering an energy balance model and use the most up-to-date ERF time series and observations of temperature and ocean heat content to constrain the ERF and ECS_{inf}. Using a range of idealized aerosol ERF evolutions, we assess the sensitivities of these estimates to the aerosol pathway. Finally, we also allow the ERF for aerosol–cloud interaction to freely evolve within the IPCC AR6 uncertainty range in the most sensitive period of 1950 to 2014 and discuss the aerosol trend and its relation to the increase in the radiative imbalance as seen from space.

2 Method

In this work ERF and climate sensitivity are estimated using a Bayesian framework with prior estimates of historical anthropogenic and natural ERF and historical observations of surface temperature and ocean heat content (OHC).

2.1 Bayesian estimation model

The Bayesian estimation model was first documented in Aldrin et al. (2012) and further developed in Skeie et al. (2014, 2018). The full model consists of a dynamic process

model with an idealized representation of the Earth's energy balance – a simple climate model (hereafter referred to as the SCM), a data model that describes how various observations are related to the process states, and a parameter model that expresses our prior knowledge of the parameters. The model is described in detail in Appendix A. The method simultaneously estimates posterior estimates (including uncertainties) of the ERFs, the ECS_{inf}, and other model parameters.

2.2 Effective radiative forcing

The prior time series for the ERF used in this study is from the IPCC AR6 (C. Smith et al., 2021; Forster et al., 2021) and the extension of these forcing time series to 2022 (Forster et al., 2023), hereafter named AR6 extended.

The IPCC AR6 provides the best estimate and the 5th and the 95th percentile of the forcing time series. The aerosol ERF is separated into ERF due to aerosol–radiation interactions (ERFari) and aerosol–cloud interactions (ERFaci). Table A1 lists the forcing components included in our estimation. The implementation of the ERF uncertainties from AR6 and AR6 extended is described in Appendix A, and the ERF priors are shown in Figs. S1 and S2 in the Supplement.

2.3 Observational data

The observational-based data series used in the Bayesian estimation model are annual hemispheric means of surface temperature (blended sea surface temperature over ocean and 2 m temperature over land), global annual OHC for 0–700 m and 700–2000 m, and an El Niño–Southern Oscillation (ENSO) index. Three different data series for surface temperature and seven different data series for OHC are used. As an ENSO index the monthly Southern Oscillation Index (SOI) is used. The observation-based data series used are listed in Table A2 and shown in Figs. S3–S5.

In the Bayesian estimation we use the temporal evolution of the reported errors for the observation-based series and estimate their magnitudes within the model, taking into account the possibilities that the reported standard errors may underestimate or overestimate the true uncertainty. For OHC, we choose to use the temporal evolution of the uncertainty from one dataset, as the reported uncertainties (Fig. S6) may not include the full uncertainties in OHC (see Appendix A). It is important to attempt to represent the full uncertainty as the OHC data have previously been shown to have a profound influence on observationally constrained climate sensitivity estimates (Johansson et al., 2015; Skeie et al., 2014).

As the representation of deep-water formation in the SCM is simplified, putting heat at the bottom layer of the model, we compare the OHC for 700 to 2000 m in observations to OHC below 700 m in the model. We do not include observations of OHC data below 2000 m due to limited observation time series and assume that these are within the uncertainties in the observed OHC.

2.4 Estimations

As a starting point, we use the baseline estimation from Skeie et al. (2018), where the IPCC AR5 time series (Myhre et al., 2013b) were used as the ERF priors and observations up to 2014 were included (Skeie18). We replace the AR5 prior with the AR6 prior and further with the AR6 extended prior. In Fig. S1 the AR5, AR6, and AR6 extended ERF priors are compared. IPCC AR5 did not provide estimates of how the uncertainties evolved in time, and in Skeie et al. (2018) we assumed that the uncertainties in ERF scaled with time and not magnitude of the forcing as in AR6. By updating the ERF prior by extending up to 2019 (Base) and 2022 (Base extended), respectively, more recent observations could also be included. When forcing priors are replaced and additional years with observations are included (Table 1), this is done stepwise as described in Appendix A and summarized in Table A3.

For each ensemble member in the Bayesian estimation, the sampled uncertainty scale factor for each ERF component is applied to the whole time series. There are hence no uncertainties in the time evolution of the ERF, identified as a limitation of the method (Skeie et al., 2018). Therefore, a range of sensitivity tests are done for the setup in Base, where aerosol ERFs from AR6 are replaced with idealized alternative pathways. Four sets of sensitivity tests are performed where the priors for ERFari and ERFaci are adjusted (Figs. S7 and S8). First, we perform a sensitivity test where the aerosol ERFs are smoothed. Thereafter we perform a second group of sensitivity tests where aerosol ERFs in different time periods are adjusted. In the third group of sensitivity tests we change the year of the strongest aerosol ERF by replacing the AR6 aerosol ERF from 1950 to a chosen year by a linear ERF. The fourth and final set of sensitivity tests is similar to the third group of sensitivity tests, but the aerosol ERFs are kept constant for the years following the end of the linear change. The entire aerosol ERF time series is scaled, so the 2019 aerosol ERF prior distribution is equal to the AR6 distribution. The baseline for the two latter groups of sensitivity tests is the smoothed aerosol ERFs. We compare the different sensitivity tests and the baseline estimation to see the effect of different aerosol ERF pathways on the posterior estimates of ECS_{inf} and ERF.

Finally, based on results from the sensitivity tests of adjusting the aerosol ERF in different time periods, we do a test where ERFaci values in 1950 and 2014 are independent of each other. We draw from the distribution of ERFaci in 1950 and use this scaling factor prior to 1950. Similarly, we draw from the distribution in 2014 and use that scaling factor thereafter. In the period between we linearly interpolate these two scaling factors. The rate of change in the ERFaci prior therefore has much larger variability than in the baseline setup.

The setup and stepwise update of the baseline estimations as well as all the sensitivity tests are summarized in Table A3.

Table 1. List of estimations performed with a description of the setup, ERF prior used, and end year. A description of the stepwise change in data as well as the priors used for estimations and all the sensitivity tests are given in Table A3.

Simulation	Description	ERF prior	End year
Skeie18	The main analysis in Skeie et al. (2018)	AR5	2014
Base	Base simulation with AR6 prior	AR6	2019
Base extended	Base simulation with AR6 extended	AR6 extended prior	2022
Sensitivity tests	ERFari and ERFaci from AR6 are modified in specific time periods (see description of each test in Table A3)	AR6	2019
Sensitivity test: ERFaci trend	ERFaci uncertainties in 1950 (and before) and 2014 (and after) independent of each other	AR6 extended	2022

3 Results

In this section we present constrained estimates of ECS_{inf}, anthropogenic ERF, and aerosol ERF using observations of OHC and surface temperature as well as prior forcing time series. First, we use observations and ERF up to 2019 and thereafter update our analysis based on data including the year 2022. We investigate the sensitivity of the posterior estimates to the prior aerosol ERF temporal evolution and finally let the ERFaci evolve more freely within the uncertainty range.

3.1 Estimations using AR6 and AR6 extended ERF time series

The starting point for the analysis is the results from Skeie et al. (2018). For Base, when the AR5 forcing prior is replaced by the AR6 prior and estimation includes data up to 2019 (Table 1), the ECS_{inf} posterior mean is 2.1 K and the 90 % confidence interval (CI) is 1.5 to 2.9 K. The posterior mean ECS_{inf} is 0.2 K higher and the 90 % CI is narrower compared to Skeie18, which only included data up to 2014.

We further extend the analysis up to 2022 using the extended AR6 ERF time series from Forster et al. (2023) (Figs. S1 and S2) and updated and extended observational time series (Table A2, Figs. S3 and S5). For this setup (Base extended) the ECS_{inf} estimate shifts to slightly larger values compared to Base, with a mean estimate of 2.2 K and the 90 % CI ranging from 1.5 to 3.0 K (Fig. 1). Each step for updating and extending the data is described Table A3, and the resulting posteriori ECS_{inf} is presented in Table S1 in the Supplement.

For the transient climate response (TCR), the posterior mean is 0.1 K higher using AR6 forcing as a prior and observations up to 2019 compared to Skeie18 with data up to 2014 (Fig. S9). In Base, the mean value is 1.5 K, and the 90 % CI is 1.1 to 2.0 K. Extending the analysis up to 2022 resulted in a slight increase in the TCR, with a mean value of 1.6 K and a 90 % CI of 1.1 to 2.1 K (Fig. S9, Table S2).

The prior and posterior distributions of the anthropogenic ERF are shown in Fig. 2. For Skeie18 with AR5 forcing prior, the posterior and prior distributions were similar in 2014, while in Base the prior and posterior distributions are quite different (Fig. 2a). The prior ERF distribution in 2014 is similar for AR5 and AR6 (Fig. 2a), while the time evolution of the prior is quite different (Fig. 2c). The posteriori distributions of the anthropogenic ERF for each step updating ERF prior and extending the data (Table A1) are shown in Table S3. From this stepwise update and extension of the data used in the estimation, the temporal evolution of the forcing pathway, when replacing AR5 with AR6 forcing prior, seems to play a large role in explaining why the prior and posterior distributions of the anthropogenic ERF for the end year are so different using AR6 forcing prior and similar using AR5 forcing prior (Fig. 2b). For Base, the posterior mean is 3.1 $W m^{-2}$, with a 90 % CI from 2.6 to 3.7 $W m^{-2}$, where the lower limit is close to the prior mean of 2.7 $W m^{-2}$ from AR6 (Table S3).

Extending the analysis further to 2022 using the AR6 extended forcing prior, resulted in a posterior mean for anthropogenic ERF of 3.2 $W m^{-2}$ and 90 % CI from 2.7 to 3.7 $W m^{-2}$, which are similar to values for 2019 using the AR6 prior (Base). The posterior distributions of anthropogenic ERF in Base (for 2019) and Base extended (for 2022) were similar despite the prior distribution being shifted to larger values in the latter (Fig. 2b).

Looking at all the individual forcing components, the Base prior and posterior distributions of the ERF in 2019 are similar for all components except for ERFaci (Fig. S10). This points to aerosols for the difference in the prior and posterior anthropogenic ERF (Fig. 2). Figure 3 shows the prior and posterior distribution of the total aerosol ERF, which is the sum of ERFaci and ERFari. In Base, the posterior values for 2019 are shifted to weaker values and the distributions are narrower compared to the AR6 prior (Fig. 3b), with a posterior mean of -0.68 $W m^{-2}$ and 90 % CI ranging from -1.1 to -0.28 $W m^{-2}$ (Table S4). Stronger aerosol ERF than the prior mean of -1.1 $W m^{-2}$ in 2019 is not supported by this analysis. Also, for Base extended, the posterior distribution for aerosol ERF in 2022 is mostly in the weaker half of the prior distribution (Fig. 3b).

However, the prior time evolutions in AR5 and AR6 are quite different for aerosol ERF (Fig. 3c). In AR5 the aerosol

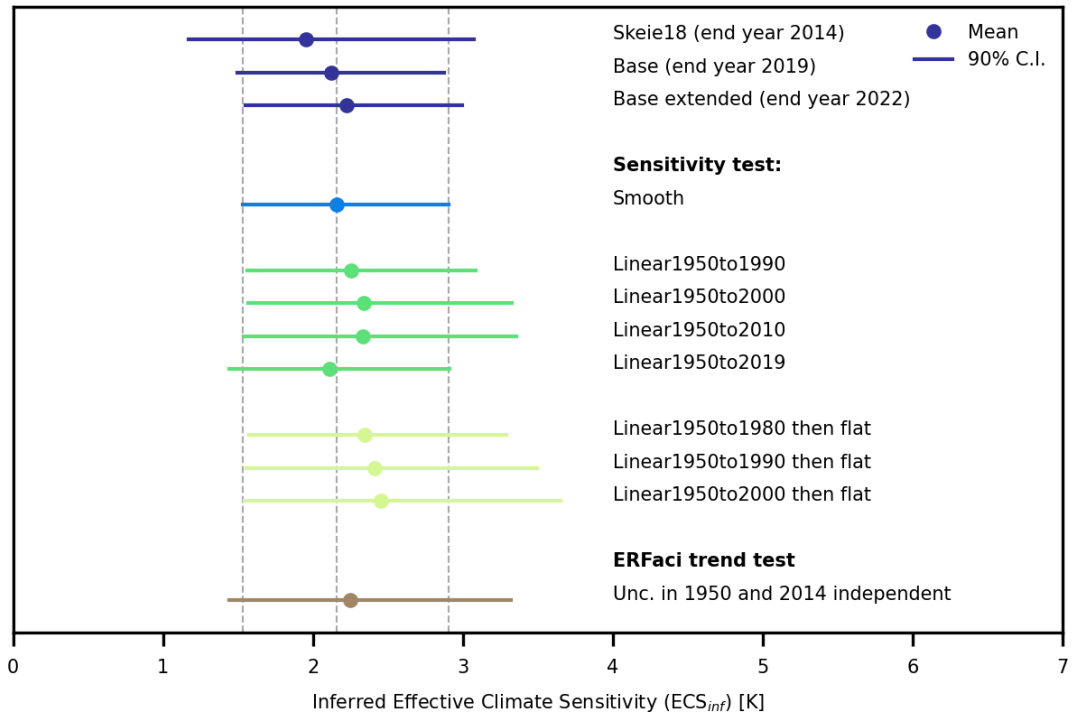

Figure 1. Posterior inferred effective climate sensitivity (ECS_{inf}) for the different analyses and sensitivity tests. The 5th to 95th percentile ranges are indicated by a solid line and the mean values as a dot. The vertical lines indicate the posterior mean value and the 90 % CI for Smooth, as it is used as a starting point for the Linear sensitivity tests shown. The posterior mean, median, and 5th and 95th percentiles are presented in Table S1, and a description of all estimations can be found in Table A3. For AR5 we use the best estimate of 2xCO2 radiative forcing from AR5, while for AR6 we use the 2xCO2 ERF corresponding to the posteriori estimate of the historical CO_2 ERF for the conversion from the climate sensitivity parameter to ECS_{inf} (see Appendix A).

ERF strengthened gradually from 1950 to around 2000 and was quite constant thereafter. In AR6 the aerosol ERF shows a steep strengthening from the 1950s to 1970s, the period when the global anthropogenic SO_2 emissions rapidly increased (Hoesly et al., 2018); then the aerosol ERF is quite stable for some decades with some interannual variability, and from around 2005 the aerosol ERF weakens in magnitude. Looking at the time evolution of the 5th percentile of total anthropogenic ERF (Fig. 2c) for Base, the prior shows a reduction in anthropogenic ERF from the 1950s until the 1970s, while in the posterior the ERF is flat over this period. The observed temperature and OHC used in the estimation do not allow for a weakening in the anthropogenic ERF in the second half of the century and hence do not allow for a stronger aerosol ERF than the prior median (Fig. 3c). A possible explanation of the weak aerosol ERF for the end year in Base and Base extended compared to the prior is that the observations do not allow for aerosol ERF in the stronger range earlier in the period (1970–1990s) and hence exclude ERF in the stronger range later in the period as well, as the uncertainty is represented as a fixed factor for the entire historical period.

3.2 Sensitivity test for aerosol ERF evolution

In the setup for Base and Base extended, no uncertainties in the time evolution of the ERF time series are included. For each ensemble member, a fixed scaling factor is used for the entire period. For Base and Base extended, the posterior aerosol ERF ended up in the weaker part of the prior distribution for 2019 and 2022, respectively (Fig. 3b). The possible explanation outlined above is that the observations do not allow for a strong aerosol ERF earlier in the period and therefore not in the later part of the period either. To investigate this potential explanation further we perform four sets of sensitivity tests where the AR6 aerosol ERF prior is replaced by idealized ERF priors (Table A3).

The prior for aerosol ERF shows some year-to-year variability (Fig. 3c). Therefore, the first test is to replace the aerosol ERF from AR6 with a smoothed forcing time series (Fig. S7a) to see the effect of the year-to-year variability in the forcing prior on the posterior estimates. With a smoothed aerosol ERF prior, the posteriori distributions of ECS_{inf}, TCR, aerosol ERF, and anthropogenic ERF are similar to Base (Figs. 1, S9, 3b, S11a, 2b, and S12a). This indicates that the posterior estimates are not sensitive to interannual variability in the forcing prior.

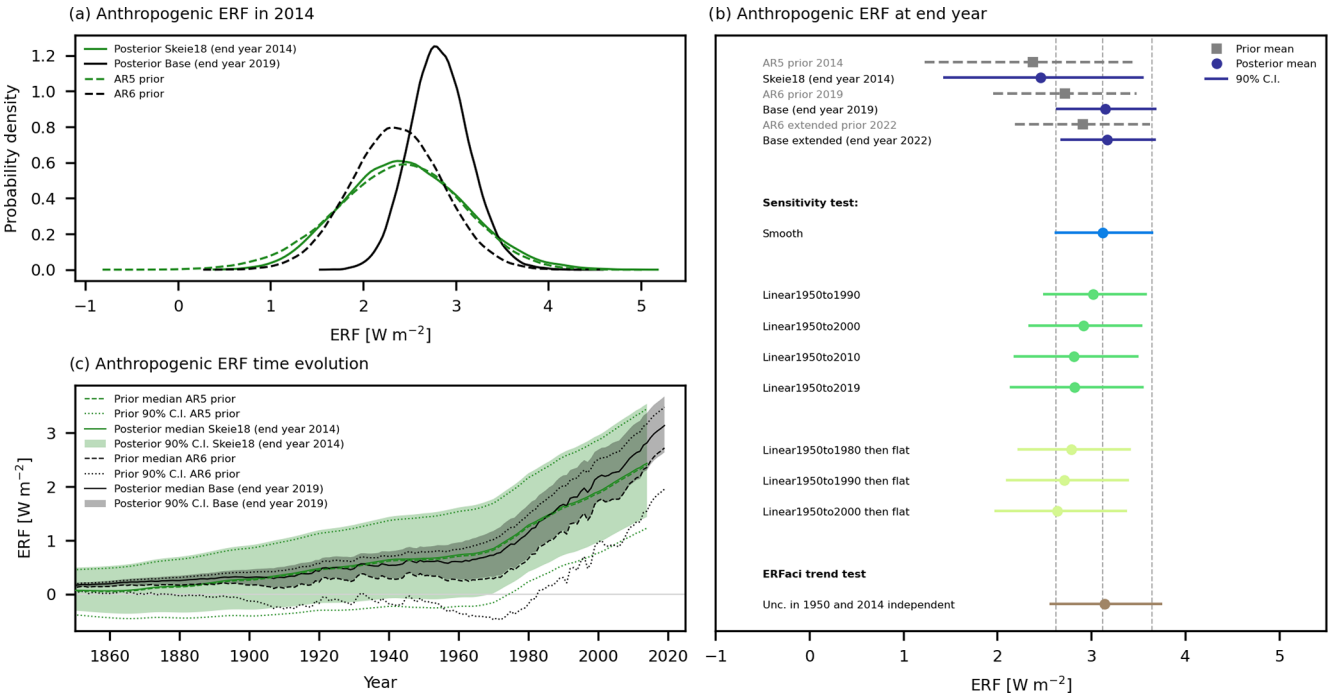

Figure 2. Prior and posterior distributions of anthropogenic ERF. In **(a)** is the probability density function of the prior (dashed line) and posterior (solid line) ERF in 2014 for Base using the AR6 prior (black) and Skeie18 using the AR5 prior (green). In **(b)** the posterior 90 % CI is indicated by a solid line and the posterior mean as a dot; the prior 90 % CI is indicated by a dashed line and the prior mean as a square. The results are shown for the end year in the analysis. In **(c)** the prior and posterior time evolutions of the anthropogenic ERF are shown for Skeie18 and Base. The underlying numbers for **(b)** are presented in Table S3.

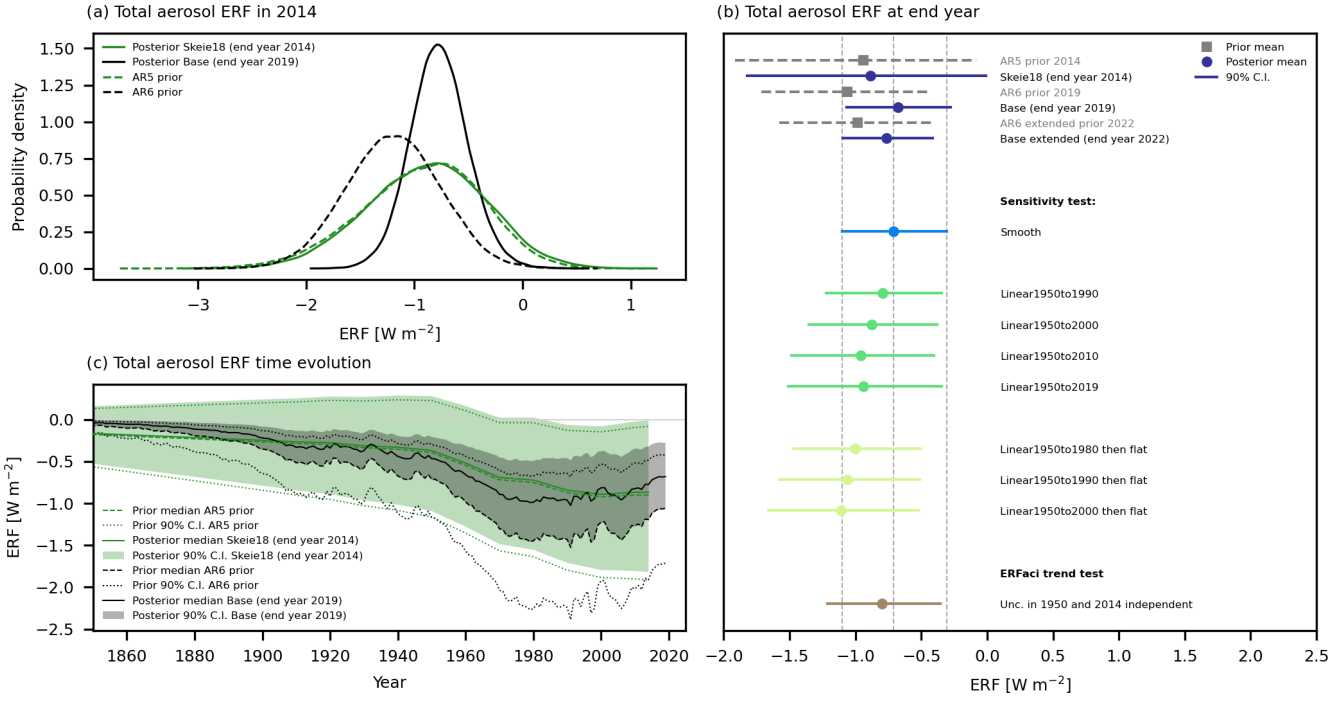

Figure 3. Same as Fig. 2, but for aerosol ERF. The underlying numbers for **(b)** are presented in Table S4.

The second group of sensitivity tests adjusts the aerosol ERF in different time periods to identify periods where the posteriori estimates are sensitive to the aerosol forcing time evolution (Fig. S7b). Adjusting the time series prior to 1950 had a minor effect on the posteriori estimates of ECS_{inf} (Table S1). Also adjusting the aerosol ERF from 2014 led to only minor changes in the posterior ECS_{inf} compared to Base. However, adjusting the aerosol forcing pathway from 1950 and onwards had a greater impact on the posteriori estimates. For the two periods 1950 to 1980 and 1980 to 2019, the difference for the 95th percentile of ECS_{inf} between the two tests performed was approximately 0.5 K (Table S1).

The third group of sensitivity tests investigates the sensitivity of shifting the year of the strongest aerosol ERF to later years. The aerosol ERF evolution from 1950 to a given year was replaced by a linear strengthening of the aerosol ERF (Fig. S7c). The smoothed AR6 aerosol ERF prior (Smooth) was used as the starting point here, as the aerosol ERF in AR6 shows large interannual variability in the early 21st century. The posteriori present-day aerosol ERF strengthened as the aerosol ERF maximum was shifted from around 1980 as in Smooth to 1990, 2000, and 2010 (Fig. 3b), and accordingly the present-day anthropogenic ERF weakened (Fig. 2b). The posteriori ECS_{inf} increased from 2.1 K in Smooth to 2.3 K in these sensitivity tests (Fig. 1). With a linear reduction of aerosol ERF from 1950 all the way to 2019, the posteriori distribution of aerosol ERF in 2019 is similar to Linear1950to2010 (Fig. 3b), but the estimated ECS_{inf} is quite different, where the posterior mean is reduced by 0.2 K (Fig. 1). Due to the shape of the aerosol ERF history, the integrated posterior aerosol ERF between 1950 and 2019 is weaker in Linear1950to2019 compared to Linear1950to2010 (Fig. S11c), and correspondingly the integrated total anthropogenic ERF is stronger in Linear1950to2019 compared to Linear1950to2010 (Fig. S12c). This further highlights the importance of the time evolution of the prior ERF and not only the present-day ERF value for constraining ECS_{inf}.

The final set of idealized sensitivity tests is similar to the linear sensitivity test, but here the aerosol ERF is kept constant for the period following the linear strengthening of the forcing. The full aerosol ERF time series is then scaled so the aerosol ERF distribution in 2019 is similar to AR6 (Fig. S7d). These aerosol ERF time series may represent a saturation of the aerosol ERF after the strongest ERF is reached, where an additional increase or decrease in aerosol or aerosol precursor emissions has only a minimal influence on the aerosol ERF. In these sensitivity tests the aerosol ERF stabilizes over the recent decades, like the AR5 prior where the aerosol forcing stabilized after the 1990s (Fig. 3c). The later the stabilization period starts, the stronger the posteriori aerosol ERF in 2019 (Fig. 3b) and the larger ECS_{inf} and TCR (Figs. 1 and S1). For the test with a linear reduction of aerosol ERF from 1950 to 2000 and a constant value thereafter, the posteriori distribution of aerosol ERF for 2019 is similar to the AR6 prior (Fig. 3b); the posteriori mean ECS_{inf} is 2.5 K and the 95th percentile is 3.6 K.

3.3 Sensitivity test adjusting the ERFaci trend

Based on the results from the sensitivity tests replacing the AR6 ERF time series with idealized aerosol ERF pathways in specific time periods, we do a test where the aerosol ERF trend is allowed to vary more than in the baseline setup. We build this test on Base extended using data up to and including 2022. We draw from the uncertainty distribution of ERFaci in 2014 and 1950 independently. Prior to 1950 and after 2014 we use the respective scaling factors, while for the period between 1950 and 2014 we linearly interpolate these two factors. An ensemble with a weak ERFaci in 1950 and a strong ERFaci in 2014 will have a different temporal pathway than a strong ERFaci in 1950 and a weak ERFaci in 2014.

The ECS_{inf} posteriori mean was similar, but the 90 % CI widened in this test compared to Base extended, with an upper value of 3.3 K compared to 3.0 in Base extended (Fig. 1). Also, the posteriori estimates of TCR with a 90 % CI of 1.1 to 2.2 K were wider compared to Base extended, with a 0.1 K higher upper limit of the 90 % CI (Fig. S1).

In Fig. 4 the distributions of the ECS_{inf} and aerosol ERF in 2022 for this sensitivity test and Base extended are shown. The joint distribution is stretched towards higher values of ECS_{inf} in this test (Fig. 4b) compared to Base extended (Fig. 4a). The posterior mean aerosol ERF in 2022 was $-0.80\,W\,m^{-2}$, with a 90 % CI of -1.2 to $-0.36\,W\,m^{-2}$ compared to the prior mean of $-0.98\,W\,m^{-2}$ and 90 % CI of -1.6 to $-0.41\,W\,m^{-2}$ (Fig. 3b). Still, the strongest aerosol ERF in AR6 extended for 2022 is not supported by this analysis even though the aerosol ERF in the latter half of the 20th century is not directly tied to the ERF in 2022.

4 Discussion

Although we test our estimation method with a wide range of highly idealized aerosol ERF pathways, our posteriori estimates of the climate sensitivities (Fig. 1) are weaker than community estimates of climate sensitivity (Forster et al., 2021; Sherwood et al., 2020) and estimates from most climate models. A total of 21 out of 42 CMIP6 models have climate sensitivities larger than the maximum 95th percentile of 3.6 K (Fig. 1) (C. Smith et al., 2021). In the following discussion, we will first relate our estimates of ECS_{inf} to the climate models' climate sensitivities. Then we will discuss the influence of the aerosol ERF pathway on our estimates and at the end how the results here relate to the Earth energy imbalance (EEI) as observed from space.

4.1 ECS_{inf} versus ECS

In this work we estimate the inferred effective climate sensitivity based on historical observations of temperature and

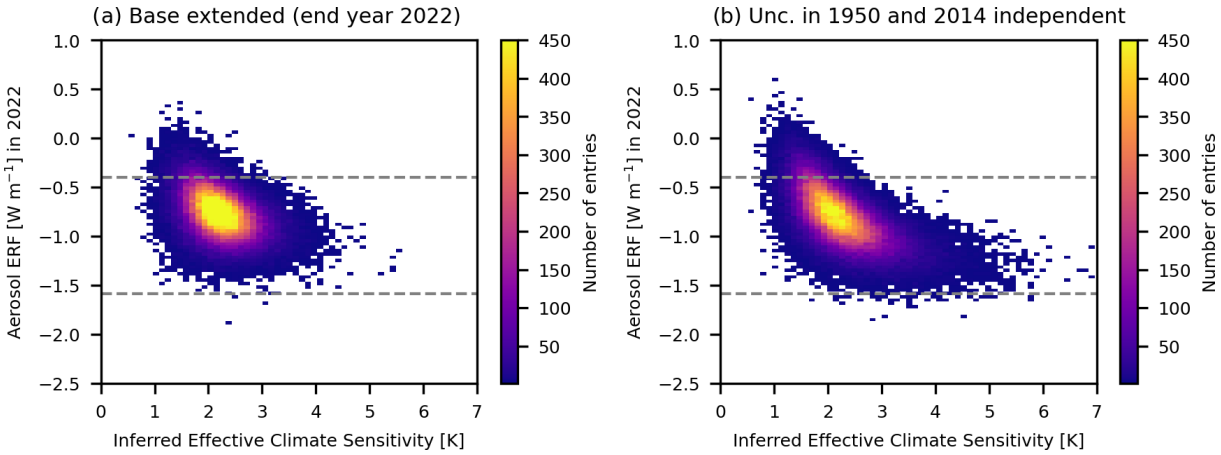

Figure 4. The joint posterior distribution of aerosol ERF in 2022 and posterior ECS_{inf} **(a)** for Base extended and **(b)** with the aerosol ERFaci uncertainties in 1950 and 2014 treated independently. The 5th and 95th percentiles in the aerosol ERF prior for 2022 are shown as horizontal dashed lines.

OHC. For calculations of climate sensitivity in climate models, the models are run with an abrupt quadrupling of the CO_2 concentrations from pre-industrial levels. Equilibrating the models requires running the model for at least thousands of years (Rugenstein et al., 2020). The climate models are instead run for a shorter period, often 150 years, and surface temperature anomalies and top-of-atmosphere (TOA) net downwelling radiative flux anomalies regressed to project the climate sensitivity, a method developed by Gregory et al. (2004) and used for CMIP6 models in Zelinka et al. (2020). This climate sensitivity is termed effective climate sensitivity (ECS) and does not include feedbacks occurring over timescales longer than 150 years. The ECS_{inf} calculated here will differ from the climate models' ECS for several reasons, which we will go through below.

First, the observed time series for global mean temperatures are blended products of measured air temperature (2 m above surface) over land and sea surface temperature over ocean, termed global mean surface temperature (GMST). In the SCM this definition of temperature change is implemented, while in climate modeling, the global mean surface air temperature (GSAT) is used for calculation of ECS. In IPCC AR6 the difference between the long-term change in GSAT and GMST was assessed to be less than 10 %, but with low confidence in the sign of the difference (Gulev et al., 2021a) as GSAT increases faster than GMST in climate models, while a limited numbers of observational studies show the opposite. To illustrate the effect of the definition of temperature on the ECS_{inf}, the probability density function of ECS_{inf} in Base is enhanced by 4 % and 10 % (Fig. 5a). We only illustrate an increase here as changes in GSAT are larger than GMST in climate models. For a 10 % increase in the temperature response, the ECS_{inf} median value increased from 2.1 to 2.3 K (Fig. 5c).

Both the historical CO_2 ERF and the ERF for a doubling of CO_2 concentration (2xCO2 ERF) are assessed with uncertainties (Forster et al., 2021), and there is considerable spread in CO_2 ERF diagnosed in climate models (Smith et al., 2020). The difference in CO_2 forcing in the climate models has implications for ECS diagnosed from the model simulations (Cess et al., 1993; Soden et al., 2018), as a larger forcing results in a larger temperature response. For illustration, for the 90 % uncertainty range of 2xCO2 ERF from IPCC AR6 (3.46–4.40 W m^{-2}) and a best estimate of the climate sensitivity parameter of 0.76 K (W m^{-2})$^{-1}$ (3 K per 3.93 W m^{-2}) (Forster et al., 2021) the ECS will increase or decrease by 0.36 K (12 %) relative to the best estimate of 3 K. In addition, the forcing strength can also change as the climate changes. The instantaneous radiative forcing of CO_2 is found to be dependent on the climatic base state and increases by 25 % for every doubling of CO_2 (He et al., 2023). This contributes to a $\sim$ 15 % to 20 % increase in climate sensitivity for every doubling of CO_2. ECS diagnosed in climate models from 4 times the CO_2 concentration will hence be larger than ECS_{inf} derived from observations over the historical period where the CO_2 concentration has only increased by $\sim$ 50 %.

The strength of the climate feedbacks can also change over time (Armour, 2017; Senior and Mitchell, 2000), and one reason for this is the so-called "pattern effect" (Stevens et al., 2016). The radiative feedbacks depend on the spatial pattern of the warming (e.g., Andrews et al., 2015), and as the spatial pattern of surface temperature evolves over time, the climate feedbacks change. From climate model simulations over the historical period, the ECS inferred from different climate realizations can differ by 0.7 K (Dessler, 2020) due to internal natural variability (Dessler, 2020). This further highlights challenges in inferring climate sensitivity from historical ob-

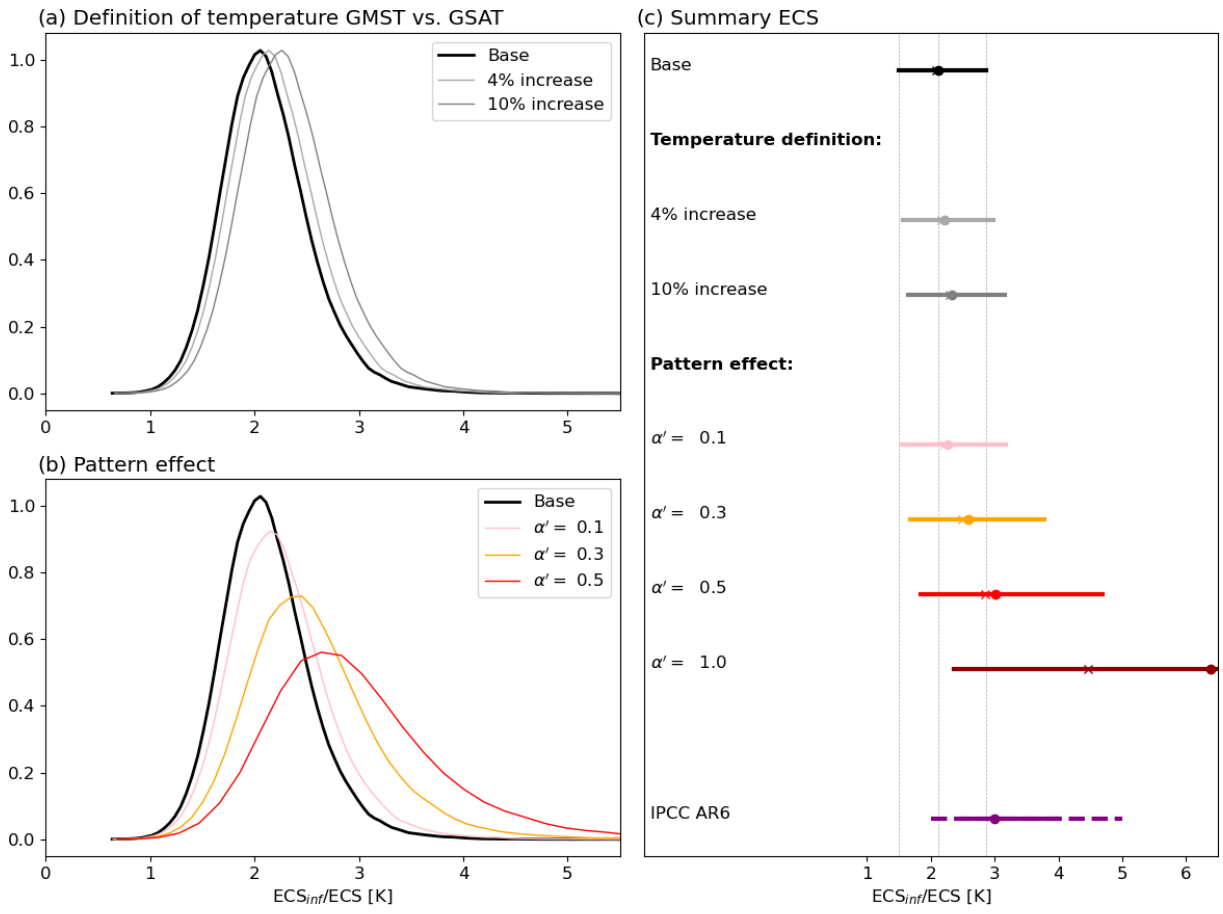

Figure 5. Illustrations of the reasons for differences between observational estimates of ECS_{inf} and effective climate sensitivity (ECS) as diagnosed from climate models. In **(a)** the influence on ECS for different definitions of temperature is illustrated. The ECS_{inf} values estimated in Base, based on observations of GMST, are enhanced by 4 % and 10 % as changes in GMST are larger than GSAT in climate models. In **(b)** different assumptions of the "pattern effect" are added to the ECS_{inf} estimate from Base. The different values for α' are given in the legend. For Base $\alpha' = 0$. In **(c)** the results are summarized by the mean value (filled circle), median value (×), and 5th to 95th percentile range as a solid line. Also indicated is the assessed best estimate of equilibrium climate sensitivity from IPCC AR6 (filled circle) and the very likely (solid line) and likely (dashed line) uncertainty range.

servations, as we only have one realization of the Earth's historical climate.

To take this time dependency of the feedbacks into account, the equilibrium climate sensitivity can be written as $ECS = -\Delta F_{2xco2}/(\alpha+\alpha')$, where α is the effective feedback parameter estimated over the historical period and α' represents the change in the feedback parameter between the historical period and the time of equilibrium for a 2xCO2 forcing (ΔF_{2xco2}). The α' factor can be calculated from Earth system models, and IPCC AR6 assessed α' to be in the range of 0.0 to 1.0 $W m^{-2} K^{-1}$ (Forster et al., 2021). The feedback parameter α [$W m^{-2} K^{-1}$] quantifies the change in net energy flux at the TOA for a given change in global temperature and represents the Planck response and all other feedbacks. In the SCM, the climate sensitivity parameter λ [$K [W m^{-2}]^{-1}$] represents these feedbacks. The relationship between the effective λ and α (as estimated based on observations over the historical period) is $\lambda = -\frac{1}{\alpha}$. To test the effect of changes in the climate feedback over time we calculate ECS from an adjusted climate sensitivity parameter $\lambda + \lambda' = -\frac{1}{\alpha+\alpha'} = \frac{\lambda}{(1-\lambda\alpha')}$. For the posteriori estimates of λ we convert to $\lambda + \lambda'$ for four different values of α' (0.1, 0.3, 0.5, 1.0) in addition to α' equal to zero as in Base, spanning the range of 0.0 to 1.0 $W m^{-2} K^{-1}$ from IPCC AR6. The probability density functions are then shifted to larger values, stretching the tail towards higher values for the climate sensitivity (Fig. 5b). A pattern effect of 0.5 $W m^{-2} K^{-1}$ shifts the ECS_{inf} mean value in Base to 3 K, which is equal to the best estimate of the ECS assessed by IPCC AR6. A stronger pattern effect of 1 $W m^{-2} K^{-1}$ gives much larger climate sensitivity estimates with a mean value of 6.4 K (Fig. 5c), but note that the values of λ now extends our prior range.

The observed sea surface temperature pattern, with a stronger warming in the western Pacific and a cooling in the

eastern Pacific, is not simulated within coupled atmosphere–ocean climate models (Fueglistaler and Silvers, 2021; Wills et al., 2022). Natural internal variability, as represented in the model, are unlikely to be the reason for the observed temperature in the Pacific, and Wills et al. (2022) point at model biases in the response to historical forcing as part of the discrepancy. Recently, using an ensemble from a single climate model with idealized step changes in aerosol emissions, Hwang et al. (2024) found that the equatorial Pacific cooled following an increase in aerosol emissions and that the cooling persisted for several decades after the aerosols were removed due to the lag in the oceanic thermal response of the aerosol forcing. Limitations in our understanding of the drivers of the observed sea surface temperature patterns and uncertainty in the strength of the "real-world" pattern effect and how it will evolve in the near future substantially increase the uncertainty about future warming (Zhou et al., 2021).

Although the temperature definition and CO_2 ERF can explain some of the differences between climate sensitivity calculated from climate models and inferred from observations, the assumptions on the pattern effect are crucial. Pattern effects within the IPCC AR6 assessed range of 0 to $1\,W\,m^{-2}\,K^{-1}$ can shift the mean value of ECS_{inf} to values larger than the upper very likely limit of 5 K from IPCC AR6. The upper limit of climate sensitivity cannot be constrained by historical observations due to the pattern effect by definition. The recognition of the pattern effect reconciled the previous discrepancies of historical constrained climate sensitivity estimates and ECS in climate models (Forster et al., 2021), and the pattern effect is a limiting factor in the quest for constraining the "true" climate sensitivity. Combining multiple lines of evidence, also including paleoclimate data, may give a stronger constraint on the ECS (Sherwood et al., 2020).

The TCR should be less influenced by the pattern effect. In Base extended the posteriori mean is 1.6 K, with a 90 % CI of 1.1 to 2.1 K. The posteriori distributions of TCR are weaker compared to the IPCC AR6 assessment (Forster et al., 2021), where the 90 % CI includes values lower than the very likely lower bound of 1.2 K from IPCC AR6 but not values greater than the likely upper bound of 2.2 K from IPCC AR6 (Forster et al., 2021) (Fig. S9).

4.2 Aerosol forcing trend

In Base, the posteriori distribution of the present-day (2019 relative to 1750) aerosol ERF was shifted to weaker values compared to the prior based on IPCC AR6, with a very likely range of -1.7 to $-0.4\,W\,m^{-2}$. The uncertainty in aerosol ERF in Base was not allowed to change over time. In the estimation, updating the aerosol forcing values based on observed temperature change and OHC, a strong aerosol forcing from the mid-20th century was prohibited (Fig. 3c) and hence a strong present-day aerosol forcing (Fig. 3b) and a weak present-day anthropogenic ERF (Fig. 2b) were excluded.

From the sensitivity test on historical aerosol time evolution, the posteriori distribution of the present-day aerosol ERF can be very different for different assumptions on the aerosol ERF time evolution (Fig. 3b). This underlines the importance of the pathways of the aerosol ERF, not only for this approach of estimating ECS_{inf} and ERFs based on historical observations, but also for climate models evaluated on historical changes and used for projections of future climate evolution. As also highlighted in Smith and Forster (2021), if the forcing is not correct, the temperature in the past and projections for the future will be biased. The climate models contributing to RFMIP and AerChemMIP showed quite variable time evolution of the diagnosed aerosol ERF (C. J. Smith et al., 2021). Using an emission to forcing relationship based on the diagnosed aerosol ERF in these CMIP6 models and a climate emulator trained on CMIP6 models, C. J. Smith et al. (2021) constrained the aerosol ERF using observed near-surface warming and the 1971 to 2018 Earth energy uptake. They estimated aerosol ERF in 2019 with a slightly narrower uncertainty range than IPCC AR6 of -1.5 to $-0.4\,W\,m^{-2}$ and a modest recovery in aerosol forcing ($+0.025\,W\,m^{-2}$ per decade) between 1980 and 2014. We find a slightly larger change in aerosol forcing of $+0.031\,W\,m^{-2}$ per decade over the same period in Base extended, slightly weaker than $+0.035\,W\,m^{-2}$ per decade in the prior. If we then let the ERFaci evolve more freely within the AR6 uncertainty range between 1950 and 2014 compared to Based extended, the trend in aerosol ERF is similar to C. J. Smith et al. (2021), with $+0.024\,W\,m^{-2}$ per decade between 1980 and 2014.

In Fig. 6, the 20-year linear trend for six different periods after 1950 is shown for Base extended and the test where ERFaci evolves more freely within the AR6 uncertainty range. As the aerosol ERF prior is quite stable from the 1970s to early 2000s (Fig. S1) and the uncertainties are tied to the uncertainty in the end year, the prior and the posterior for the aerosol ERF trend are narrow and close to zero in this period. When the ERFaci is allowed to evolve more freely within the IPCC AR6 range, both the prior and the posterior 90 % CI for the aerosol ERF trend are broadened (Fig. 6). For the two earliest periods, 1950–1969 and 1960–1979, the posterior trends are weaker than in the prior. This is the period where the global anthropogenic SO_2 emissions rapidly increased before peak emissions around 1980 (Hoesly et al., 2018). For the latest period, 2009–2019, the posterior aerosol ERF trend is also weaker than in the prior, in the weaker range of C. J. Smith et al. (2021), and similar to Albright et al. (2021) with increased variance, as presented in Quaas et al. (2022). Keep in mind that in this test, the ERFari is still tied to the AR6 ERFari pathway, as is ERFaci post-2014. For comparison, the median aerosol ERF trend of $0.1\,W\,m^{-2}$ per decade for the 2000 to 2019 period is a third of the increase in CO_2 ERF over the same period.

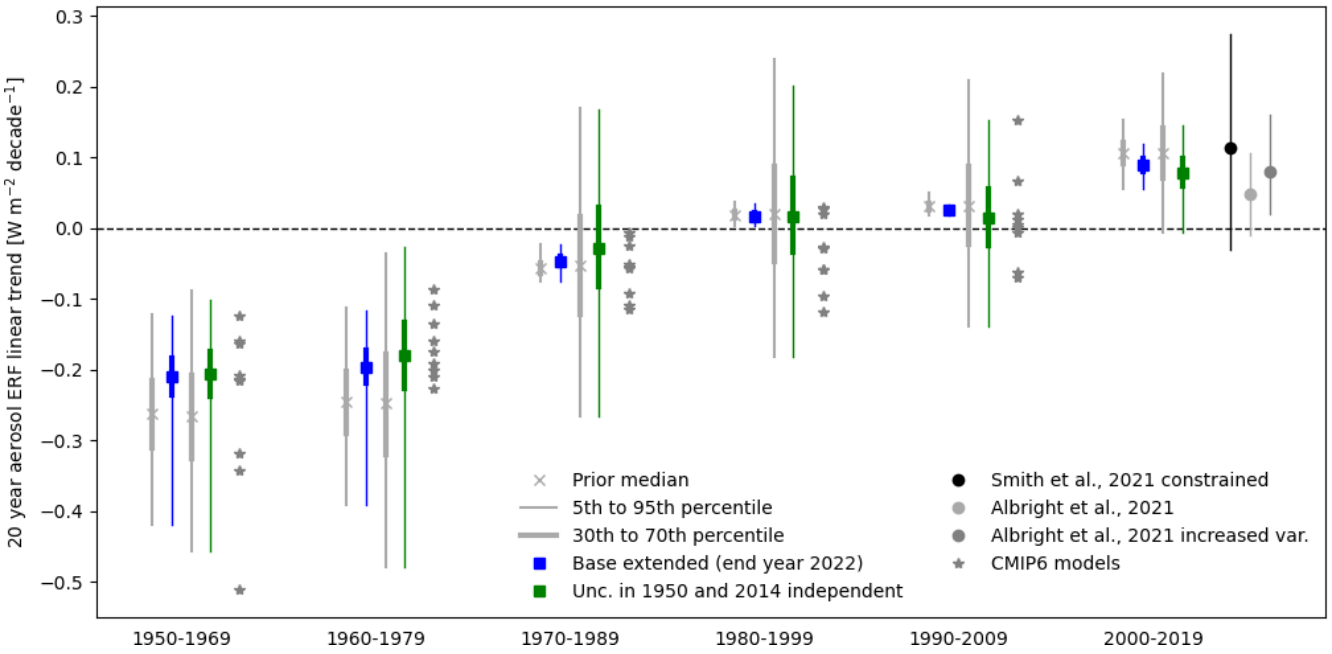

Figure 6. The 20-year aerosol ERF linear trend for six different periods. The posterior aerosol ERF trends are shown for Base extended (blue) and the test with independent uncertainties in 1950 and 2014 (green), with the corresponding prior distribution plotted in gray to the left of the posterior. The median (crosses for prior and squares for posterior), 30th to 70th percentiles, and 5th to 95th percentiles are shown. For the first five time periods, the linear trend in the ERF diagnosed from nine CMIP6 models in C. J. Smith et al. (2021) is shown as stars, and the linear trends are calculated on smoothed time series of ERF. For the last period (2000 to 2019) the mean and the 5th and 95th percentiles presented in Quaas et al. (2022) from Albright et al. (2021) and C. J. Smith et al. (2021) are shown.

Also shown in Fig. 6 are trends calculated from aerosol ERF diagnosed within CMIP6 models (C. J. Smith et al., 2021). The spread in trend is large in all periods, and for the 1960 to 1979 period the modeled ERF trends are in the weaker range of the priors and more consistent with our posterior distributions. In the 1980 to 1999 period most of the CMIP6 models have a negative aerosol ERF trend, while the posteriori mean is close to zero but the 90 % CI is wide.

4.3 Energy imbalance

The trend in the Earth energy imbalance (EEI) can be estimated based on satellite retrievals (Loeb et al., 2018a) and can in principle give additional information on the aerosol ERF pathway. The EEI is the net radiative flux at the top of atmosphere (TOA), and it determines the evolution of global temperature change. For a positive imbalance at the TOA, less energy is leaving than entering the system, heat is stored in the system, and surface temperature will increase to restore the energy balance at TOA. The EEI is the portion of the radiative forcing that has not yet been responded to (Hansen et al., 2005). In a linear framework this can be written as $\mathrm{EEI} = \mathrm{ERF} + \alpha \Delta T$, where α is the net total feedback parameter [$\mathrm{W\,m^{-2}\,K^{-1}}$], which represents the combined effect of the various climate feedbacks. In this study the climate sensitivity parameter $\lambda = -1/\alpha$ represents these feedbacks.

From the TOA Earth radiation budget from the Clouds and the Earth's Energy System (CERES) data, the trend in EEI can be analyzed (Loeb et al., 2018a). As the absolute values of the radiation fluxes are too uncertain, these are anchored to the mean of observed rate of heat gain, mainly storage of heat in the ocean over a reference period (2005 to 2015) (Loeb et al., 2018b). The trend in CERES data can be used as additional information in our Bayesian setup, as the trend in EEI is independent of the OHC data that are already included in our estimation. Here, however, we only compare the posterior estimates of EEI with the CERES EEI trend.

Figure 7a shows the EEI from Base extended from the forced temperature response as well as the temperature response including ENSO variability. Including ENSO, the median value averaged over the period 2006 to 2020 of $0.74\,\mathrm{W\,m^{-2}}$ is in good agreement with the $0.76 \pm 0.2\,\mathrm{W\,m^{-2}}$ from von Schuckmann et al. (2023), which also holds for the longer period 1971 to 2020 with a median value of $0.49\,\mathrm{W\,m^{-2}}$ in this study and $0.48\,\mathrm{W\,m^{-2}}$ in von Schuckmann et al. (2023). This is as expected as observational-based time series of OHC used in this study are included in the assessment of von Schuckmann et al. (2023) (see also Fig. S4). For the trend in EEI, the forced EEI with and without the ENSO response is $0.2\,\mathrm{W\,m^{-2}}$ per decade from 2005 to 2022. This is clearly weaker than the linear trend for the 12-month running mean CERES EEI of $0.44\,\mathrm{W\,m^{-2}}$ per

decade (Fig. 7a). Adding the ENSO temperature response enhanced the year-to-year variability in EEI, but the variability is weaker than in CERES (Fig. 7a), which shows pronounced interannual variability driven primarily by clouds (Loeb et al., 2018a, 2021), variability that an SCM would not capture.

Although the posteriori results of EEI averaged over the period 2005 to 2019 for the baseline as well as all sensitivity tests are within the CERES uncertainties from Loeb et al. (2021) (Fig. 7b), there are several possible reasons why the posteriori EEI does not reproduce the CERES trend.

From the linearized equation of the EEI, the EEI will increase with time if ERF increases at a greater rate than $\alpha \Delta T$. Over the last decades, there has been rapid reduction of SO_2 emissions, especially over China (Zheng et al., 2018), contributing to an increase in the total anthropogenic forcing trend (Forster et al., 2023). If the trend in ERF is wrongly implemented, this will influence our EEI estimate. The idealized aerosol experiments, changing the time evolution of aerosol ERF, strongly influence the trend in EEI (Fig. 7b and c). The posterior EEI trend increases by $\sim 50\,\%$ in sensitivity tests, with weaker aerosol ERF towards 2019 compared to Base, but is still in the lower range of the CERES trend. Sensitivity tests with strengthening of the aerosol ERF all the way to 2019 as well as constant aerosol ERF after the year 2000 resulted in a very weak EEI trend from 2005 to 2019, less consistent with CERES data. These results suggest that a weakening of the aerosol ERF has contributed to the trend in EEI as observed by CERES. Other studies also find a contribution of weakened aerosol ERF to the EEI trend observed by CERES (Raghuraman et al., 2021; Hodnebrog et al., 2024). The trend in EEI from CERES is dominated by an increase in absorbed solar radiation with a dominant contribution from clouds (Loeb et al., 2021), hinting at a possible important role of either aerosol–cloud interactions or cloud feedbacks. However, from the CERES data alone it is difficult to separate the ERFaci from the cloud feedback (Loeb et al., 2021; Raghuraman et al., 2023).

As discussed above, the feedback parameter can change over time but is assumed to be constant in our approach. As the climate feedbacks are dependent on the pattern of the temperature change, this effect must be included in EEI reconstructions to match observed EEI from CERES (Zhou et al., 2021). Andrews et al. (2022) indicated that the pattern effect might have been particularly strong in recent decades and waning post-2014. The possibility that the feedbacks have changed over the recent decades relative to what is estimated in our approach using observations over a longer period is not included in our methodology.

The rate of ocean heat gain is a key component for the quantification of the EEI. In our method the information on EEI trend is taken from the OHC data used. Studies investigating the trend in several different OHC datasets find a weaker trend than in CERES (Li et al., 2023; Minière et al., 2023), but Minière et al. (2023) highlighted the overlapping uncertainties in both methods for assessing the EEI trends and the challenges of assessing trends over such a short period.

The trend in EEI can be implemented in our estimation method to give an additional constraint on the recent forcing time evolution. The two sensitivity tests with weaker aerosol ERF towards 2019 strongly change the trend in EEI (Fig. 7b) but had a limited influence on the posteriori ECS estimate (Table S1). Note that the end year for our estimation is 2022, meaning that the analysis does not include the rapid increase in EEI from CERES data in 2023 (Fig. 7) or the record high temperatures in 2023 (Voosen, 2024).

5 Conclusions

We have used the most up-to-date ERF time series, observations of temperature change, and observations of ocean heat content in a Bayesian framework to estimate climate sensitivity, aerosol forcing, and aerosol forcing pathway. Aerosol ERF is the largest contributor to the uncertainties in the total anthropogenic ERF (Forster et al., 2021, 2024). As prior knowledge of the uncertainties in the time evolution of aerosol ERF is lacking, we use a range of idealized aerosol ERF time series to investigate the sensitivity of our observational-based estimates to the assumed aerosol pathway.

Our estimate of climate sensitivity is the inferred climate sensitivity, and it only includes feedbacks that have come into play over the historical period considered. The historical warming pattern favors lower climate sensitivity values than what is expected from long-term increases in CO_2 concentrations from climate model simulations (Andrews et al., 2018). The ECS_{inf} does not include this so-called pattern effect. If a pattern effect of $0.5\,W\,m^{-2}\,K^{-1}$ (the central estimate in IPCC AR6) is added to our Base estimate, the climate sensitivity estimate is almost identical to the IPCC AR6 very likely range of 2 to 5 K, with a best estimate of 3 K (Forster et al., 2021). The pattern effect limits historical observations to constraining the upper end of climate sensitivity (Sherwood et al., 2020; Armour et al., 2024). For near-term climate policy that aims for net zero emissions by mid-century (UNFCCC, 2015) the ECS_{inf} might be as relevant as climate sensitivity estimates that consider climate feedbacks over longer timescales. Furthermore, both CO_2 forcing (He et al., 2023) and feedbacks might be climate-state-dependent (Bloch-Johnson et al., 2021) and therefore differ between high forcing scenarios (as 2 or 4xCO2) and near-term net zero emission scenarios.

The ECS_{inf} estimate is dependent on the aerosol pathway. The upper 95th percentile of ECS_{inf} differs by 1.1 K for the different sensitivity tests, and the ECS_{inf} is most sensitive to the aerosol ERF pathway between 1950 and 2014. Allowing ERFaci to evolve more freely within the AR6 uncertainties between 1950 and 2014 and using forcing time series and observational data up to and including 2022, the mean ECS_{inf}

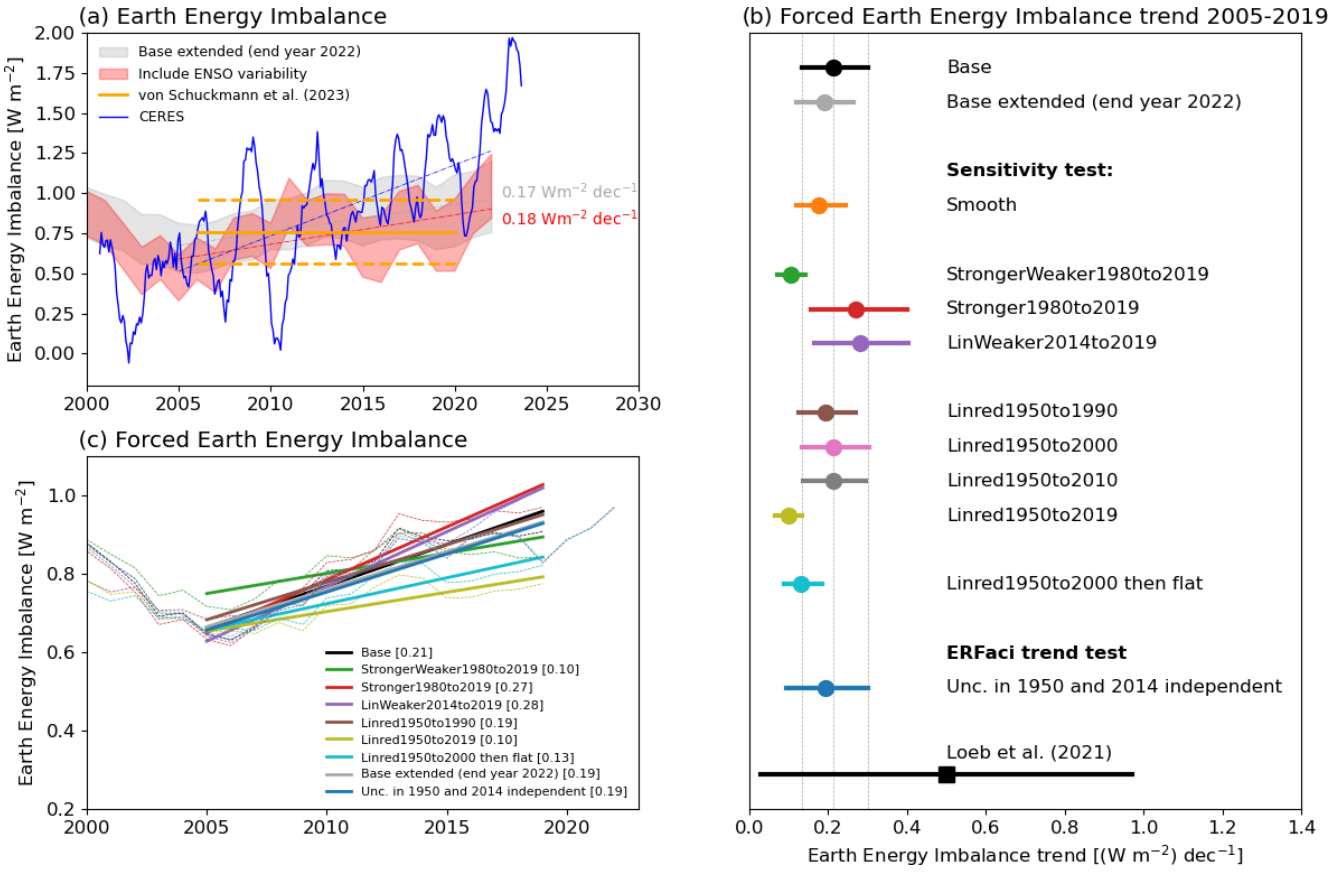

Figure 7. Posterior Earth energy imbalance and Earth energy imbalance trend. In **(a)** the gray shading shows the 5th to 95th percentile of the posteriori EEI for the forced temperature response, while the red shading shows the posteriori EEI including ENSO variability for Base extended. The dashed gray and red lines indicate the least-squares linear fit for the posterior median of EEI without and with ENSO variability included for the period 2005 to 2022, and the trends over this period are indicated in the plot. The orange lines are the EEI from von Schuckmann et al. (2023) of 0.76 W m^{-2} (solid line) ± 0.2 W m^{-2} (dashed lines) for the 90 % confidence interval for the period 2006 to 2020. CERES data are shown as a 12-month running mean in blue (Loeb et al., 2018a) (including data for January 2024) and the least-squares linear fit from 2005 to 2022 (dashed blue line). In **(b)** the posteriori forced EEI trend over the period 2005 to 2019 is shown for the 5th to 95th percentile as a solid line, with the median value as a dot. At the bottom the mid-2005 to mid-2019 estimates of the trend for the net CERES TOA energy flux of 0.50 ± 0.47 W m^{-2} per decade (90 % confidence interval) from Loeb et al. (2021) are indicated with a black square and a solid line. In **(c)** the posteriori median of the forced EEI from 2000 onwards is shown for selected sensitivity tests as annual values (dashed lines), and the linear trend from 2005 to 2019 is shown as a solid line. The trends in EEI over this period are indicated in the legend as W m^{-2} per decade.

is 2.3 K with a 90 % CI from 1.4 to 3.4 K. The estimate is shifted to larger values compared to our estimates where the aerosol pathways are more fixed, with a mean ECS_{inf} of 2.1 K (90 % CI: 1.5 to 2.9) with the AR6 ERF prior and observations to 2019 in Base and 2.2 K (90 % CI: 1.5 to 3.0) with the AR6 extended ERF prior and observations to 2022 in Base extended.

The present-day posteriori distribution of the aerosol ERF is strongly influenced by the different aerosol pathways. As the prior in Base is tied to the present-day ERF and the observations do not allow for decreasing total anthropogenic ERF in the 1950s to early 1970s, the present-day aerosol ERF shifts to more negative values when the prior for the ERF in the 1960–1970s is weakened in the sensitivity tests. Also, when the historical ERFaci is not tied to the present-day aerosol forcing, the negative aerosol ERF trend in the 1950s to 1970s is weakened compared to the prior. Stronger aerosol forcing than around −1.4 W m^{-2} in the 1960s and 1970s, the period leading up to the peak SO_2 emissions (Hoesly et al., 2018), is less consistent with observations. Over the more recent period, the pathways with a weakening of the aerosol ERF are more consistent with observations of the Earth's energy imbalance from space from CERES since 2005. Currently, observations on OHC constrain the estimated EEI in our method. Future work can implement the trend in EEI from CERES as an additional constraint in observational-based estimation of climate sensitivity, aerosol ERF, and aerosol ERF pathways.

For assessing future climate change, evaluating historical climate change is crucial and hence knowledge of how the different drivers have changed over time is critically important. In previous literature, the focus has mostly been on present-day aerosol forcing relative to pre-industrial. Better knowledge of the historical aerosol ERF pathway is, however, needed, not only related to how aerosol ERF has changed over the recent decades (Lund et al., 2023; Quaas et al., 2022) but also further back in time. For future work, prior uncertainties in the time evolution of aerosol ERF based on expert judgment should be implemented considering uncertainties in historical aerosol and aerosol precursor emissions, as well as uncertainties in the physical processes of aerosol–radiation and aerosol–cloud interactions.

Appendix A

In this section, additional information on the methods is presented.

A1 Model

The core of the model framework is a simple climate model (SCM), which is a deterministic energy balance and upwelling–diffusion model (Schlesinger et al., 1992; Schlesinger and Jiang, 1990; Sandstad et al., 2024). The model calculates annual hemispheric near-surface temperature change (blended sea surface temperature and surface air temperature over land) and changes in global ocean heat content (OHC) as a function of ERF time series. The output from the SCM, the time series of temperature and OHC, can be written as $\boldsymbol{m}_t(\boldsymbol{x}_{1750:t}, \boldsymbol{\theta})$, where $\boldsymbol{x}_{1750:t}$ represents the ERFs from 1750 until year t, which are the true, but unknown, input values to the SCM. The true but unknown parameters of the SCM are represented by $\boldsymbol{\theta}$, which is a vector of seven parameters, where one of these is the climate sensitivity parameter (λ). The other parameters determine how the heat is mixed into the ocean (e.g., mixed layer depth, air–sea heat exchange coefficient, vertical diffusivity in the ocean, and upwelling velocity).

The true state of some central characteristics of the climate system in year t can be written as $\boldsymbol{g}_t = \boldsymbol{m}_t(\boldsymbol{x}_{1750:t}, \boldsymbol{\theta}) + \boldsymbol{n}_t$, where $\boldsymbol{n}_t$ is a stochastic process, with three terms representing long-term and short-term internal variability and model error. For the short-term internal variability, the Southern Oscillation Index is used to account for the effect of the El Niño–Southern Oscillation (ENSO) on the temperature. For the long-term internal variability, the dependence structure is based on a control simulation from a CMIP5 model (Skeie et al., 2014). This term will also represent other slowly varying model errors due to potential limitations of the SCM and the ERF time series. The last error term accounts for more rapidly varying model errors.

For $\boldsymbol{g}_t$ corresponding long-term observational data are available with individual error terms. Data on surface temperatures are considered separately for the Northern and Southern Hemisphere and OHC separately for 0–700 m and below 700 m. For each of the elements of $\boldsymbol{g}_t$ several corresponding observational-based data series are available (Table A1). To gain as much information as possible, we use several datasets for the same physical quantity simultaneously.

The model parameters ($\boldsymbol{\theta}$) and the ERF time series ($\boldsymbol{x}_{1750:t}$) are given prior distributions, and we apply a Bayesian approach and use Markov chain Monte Carlo techniques to sample from the posterior distribution.

In the SCM the climate sensitivity is represented as a climate sensitivity parameter (λ). λ is multiplied by the ERF for a doubling of CO_2 (2xCO2) to present the climate sensitivity as ECS_{inf}. Here we use the 2xCO2 corresponding to the posterior estimate of CO_2 ERF for the conversion from λ to ECS_{inf}, while in previous work CO_2 forcing was included in the combined greenhouse gas forcing time series and the best estimate of 2xCO2 from AR5 (Myhre et al., 2013b) was used (Skeie et al., 2018). The TCR is calculated using the SCM with the joint posteriori distributions of the parameters forced with an ERF time series of 1 % increase per year in CO_2 concentration until a doubling of CO_2 is reached. The ERF time series used is consistent with the forcing prior used and hence different for AR5 and AR6 priors (Forster et al., 2021). If we use an ERF time series corresponding to the posterior of the CO_2 ERF, the posteriori distribution of the TCR is similar to using the best estimate of the CO_2 ERF time series (Fig. S13). Also, for ECS_{inf}, the probability density function is similar using a fixed factor and a factor corresponding to the posterior CO_2 ERF for the conversion from λ to ECS_{inf} (Fig. S13).

A2 Effective radiative forcing

How the ERF uncertainties from IPCC AR6 and AR6 extended are implemented is described below and summarized in Table A1.

For most of the forcing components, the relative uncertainty is symmetrical and constant in time, and we assume a normal distribution for these components. For the forcing components with a skewed 90 % confidence interval presented in AR6, the uncertainty in the forcing is implemented as a combination of two normal distributions as in AR6. The asymmetric uncertainty ranges and the fractional uncertainty were determined by considering ranges below and above the best estimate separately, by dividing the 5th percentile by the best estimate to derive the lower uncertainty range and the 95th percentile by the best estimate to determine the upper range, treating them as two halves of a Gaussian distribution.

In IPCC AR6 the forcing time series for aerosol–radiation interactions (ERFari) was constructed using a linear relationship between ERFari and emissions of SO_2, BC, OC, and NH_3 for sulfate, black carbon, organic carbon, and nitrate aerosols, respectively (C. Smith et al., 2021). The emission to forcing coefficients were based on multi-model results from

Table A1. Forcing components included in the estimations, their relative uncertainties, and a description of the distribution. The forcing time series, uncertainties, and distributions are implemented as in IPCC AR6 (Forster et al., 2021). The uncertainties are presented as percentages: (best − pc05)/best and (best − pc95)/best, where "best" is the best estimate, and pc05 and pc95 are the 5th and 95th percentile, respectively. The 90 % uncertainty is symmetrical if only one number is presented, and if not otherwise stated, the uncertainties are constant in time. If the uncertainties in AR6 extended (Forster et al., 2023) were updated, this is presented in parentheses in the table.

Forcing components	Uncertainties [%]	Distribution
co2	12 %	Normal
ch4	20 %	Normal
n2o	16 %	Normal
other_wmghg	19 % (19 % in 2022)	Normal (normal, not constant in time)
o3	50 %	Normal
h2o_stratospheric	100 %	Normal
Contrails	67 % lower, 69 % upper (55 % lower, 70 % upper)	Two normal
aerosol–radiation_interactions	119 % in 2019 (99 % in 2022)	Normal, not constant in time
aerosol–cloud_interactions	72 % lower, 70 % upper in 2019 (74 % lower, 70 % upper in 2022)	Two normal, not constant in time
bc_on_snow	100 % lower, 125 % upper	Two normal
land_use	50 %	Normal
Solar	50 % of the amplitude of the solar cycle + a linear 1750 to 2019 trend of $\pm 0.07\,\mathrm{W\,m^{-2}}$ (5 %–95 %)	Sum of two independent normal distributions
Volcanic	25 %	Normal

Myhre et al. (2013a) and rescaled so the total ERFari of $-0.3 \pm 0.3\,\mathrm{W\,m^{-2}}$ for present day in the assessment is preserved. The relative uncertainty of ERFari is not constant in time, but it is symmetrical. To get the same 5th and 95th percentiles as in AR6 for the ERFari time series, we assume a normal distribution and correct the uncertainties by a constant for each year to match the historical uncertainties from AR6.

The forcing time series for the aerosol–cloud interactions (ERFaci) in AR6 are based on fits to 11 CMIP6 models with historical time-varying ERFaci of a logarithmic function of emissions of SO_2, BC, and OC (C. Smith et al., 2021). A 100 000-member ensemble was drawn, and the median of this ensemble was scaled to the assessed value for present-day ERFaci in AR6. The 90 % confidence interval for ERFaci is unsymmetrical and not constant in time, and hence the left and the right halves of the prior distribution are modeled by the left and the right halves of two, possibly different, normal distributions. These normal distributions are different from one year to another.

For implementing the solar forcing, a 0.50 fractional uncertainty was applied to the amplitude of the solar cycle, and a linear 1750 to 2019 trend of $\pm 0.07\,\mathrm{W\,m^{-2}}$ (5 %–95 %) range was added to this to represent the uncertainty in the change in the underlying solar forcing of $0.01\,\mathrm{W\,m^{-2}}$, as was done in generating the ERF time series uncertainties in AR6 (C. Smith et al., 2021).

In the SCM, the ERFs are split on hemispheres for ozone, aerosol–radiation interactions, aerosol–cloud interactions, and land use. This split is constant in time, and for ozone it is calculated from multi-model results of ozone forcing time series from CMIP6 (Skeie et al., 2020) and land use and aerosols from ERF diagnosed from CMIP6 models (Smith et al., 2020).

A3 Observational data

Table A2 lists all the observational-based time series used in the estimation. As described in the Method section, we only use the temporal profile of the reported error and estimate the magnitude within the model. For OHC we choose to use the temporal development of the uncertainty from Domingues et al. (2008) for all time series as the reported uncertainties (Fig. S6) may not include the full uncertainties in OHC.

Table A2. Observation-based time series used in the estimation. What is used for the updated time series is in parentheses.

Name	Full name	Period of record	Domain	Reference	DOI/link	Date of download
Temperature						
NOAA	NOAAGlobalTemp v5.0.0 (v5.1.0)	1880–2019 (1850–2022)	NH, SH	Vose et al. (2021)	https://www.ncei.noaa.gov/products/land-based-station/noaa-global-temp	23 November 2021 (21 June 2023)
HadCRUT5	HadCRUT.5.0.1	1850–2019 (1850–2022)	NH, SH	Morice et al. (2021)	https://www.metoffice.gov.uk/hadobs/hadcrut5/	23 November 2021 (21 June 2023)
GISTEMP	GISTEMP v4	1880–2019 (1880–2022)	NH, SH	(Lenssen et al., 2019; GISTEMP-Team, 2023)	https://data.giss.nasa.gov/gistemp/	23 November 2021 (20 June 2023)
OHC						
NCEI-Levitus	Levitus/Lev12-NCEI/NCEI	1955–2019 (1955–2022)	OHC0–700 m, OHC700–2000 m	(Levitus et al., 2012)	https://www.ncei.noaa.gov/data/oceans/woa/DATA_ANALYSIS/3M_HEAT_CONTENT/DATA/basin/yearly/h22-w0-700m.dat https://www.ncei.noaa.gov/data/oceans/woa/DATA_ANALYSIS/3M_HEAT_CONTENT/DATA/basin/yearly/h22-w0-2000m.dat https://www.ncei.noaa.gov/data/oceans/woa/DATA_ANALYSIS/3M_HEAT_CONTENT/DATA/basin/pentad/pent_h22-w0-2000m.dat Used the pentadal average up to 2008 and the yearly data thereafter for below 700 m. https://www.ncei.noaa.gov/access/global-ocean-heat-content/	23 November 2021 (20 June 2023)
PMEL	PMEL/JPL/HIMAR	1993–2019[a] (1993–2022)	OHC0–700 m, OHC700–2000 m	(Lyman and Johnson, 2014)	Downloaded from reference in Table 2.SM.1 – data table in AR6 (Gulev et al., 2021b) https://oceans.pmel.noaa.gov/	10 December 2021 (11 July 2023, e-mailed from John Lyman)
Domingues	CSIRO/ACE CRC/IMAS-UTAS	1970–2019 (1970–2022[b])	OHC0–700 m	(Domingues et al., 2008)	http://www.cmar.csiro.au/sealevel/thermal_expansion_ocean_heat_timeseries.html	3 May 2022, e-mailed from Domingues
JMA-Ishii	MRI/JMA – Ishii	1955–2019 (1955–2022)	OHC0–700 m, OHC700–2000 m	(Ishii et al., 2017)	https://www.data.jma.go.jp/gmd/kaiyou/data/english/ohc/ohc_global_1955.txt https://www.data.jma.go.jp/gmd/kaiyou/english/ohc/ohc_global_en.html	17 December 2021 (21 June 2023)
IAP-Cheng	IAP/CAS	1955–2019 (1955–2022)	OHC0–700 m, OHC700–2000 m	(Cheng et al., 2017, 2019a, b, 2020, 2022)	http://www.ocean.iap.ac.cn/ftp/images_files/IAP_OHC_estimate_update.txt	10 December 2021 (9 January 2023)
Open-OHC	Open-OHC (OPEN-OHCv1.1.2)		OHC0–700 m, OHC700–2000 m	(Su et al., 2020)	https://raw.githubusercontent.com/scenty/OPEN-OHC/refs/heads/master/OPEN-OHCv1.1.1.txt	10 December 2021 (e-mailed from Wenfang Lu, 1 August 2023)
EN4	EN4.2.1/MetOffice/Good et al. (EN.4.2.2.c14/MetOffice)	1955–2019[a] (1955–2022)	OHC0–700 m, OHC700–2000 m	(Good et al., 2013; Gouretski and Cheng, 2020; Cheng et al., 2014)	Downloaded from reference in Table 2.SM.1 – data table in AR6 (Gulev et al., 2021b) https://climate.metoffice.cloud/ocean_heat.html	4 January 2022 (data e-mailed from Rachel Killick, 25 July 2023 and 1 August 2023)
SOI						
SOI	Southern Oscillation Index, Bureau of Meteorology, Australia				http://bom.gov.au/climate/enso/soi_monthly.txt	23 November 2021 (23 June 2023)

[a] Data available until 2018, with data extended from 2018 to 2019 using the average increase in the other available series from 2018 to 2019. [b] Data available until 2021, with data extended from 2021 to 2022 using the average increase in the other available series from 2021 to 2022.

https://doi.org/10.5194/esd-15-1435-2024

A4 Estimation

As a starting point we use the main analysis in Skeie et al. (2018). Stepwise, we updated the observational-based time series for surface temperature and ocean heat content, then replaced the IPCC AR5 forcing time series by the IPCC AR6 time series (Forster et al., 2021) with end year 2014 before extending the data used in the estimation to year 2019. For a better representation of the distribution of heat in the ocean, the priors for two of the parameters in the SCM are widened compared to what was used previously (Aldrin et al., 2012): the vertical velocity and upwelling rate as well as the polar parameter with a new uniform prior of $[0.55, 7]$ and $[0.161, 2]$, respectively. When replacing the ERF prior with the extended ERF time series (Forster et al., 2023) and adding additional years in the observations, a stepwise replacement and extensions of observations and forcings are performed here as well.

Table A3 lists all the different estimations performed in this study.

Table A3. List of estimations performed with a description of the setup, forcing prior used, and end year of observational data used.

No.	Simulation	Description	ERF prior	End year
1	Skeie18, AR5 prior	The main analysis in Skeie et al. (2018).	AR5	2014
2	Update obs. end year 2014	Same as no. 1 but use updated observational-based data series.	AR5	2014
3	Replace AR5 prior with AR6	Same as no. 2 but replace AR5 ERF priors with AR6 ERF priors.	AR6	2014
4	End year 2019	Same as no. 3 but extend from 2014 to 2019.	AR6	2019
5	Base	Same as no. 4 but with new priors for the upwelling velocity $[0.55, 7]\,\mathrm{m\,yr^{-1}}$ and the polar parameter $[0.161, 2]$; both priors are uniform as before (Aldrin et al., 2012).	AR6	2019
	Sensitivity test	For all sensitivity tests below, the ERFari and ERFaci from IPCC AR6 are modified in specific time periods.		
6	Smooth	As no. 5, but ERFari and ERFaci smoothed using locally weighted scatterplot smoothing in the Python statmodels module over the entire time period.	AR6	2019
			AR6	2019
7	Linear1750to1900	As no. 5, but a linear ERFari and ERFaci from 1750 to 1900.	AR6	2019
8	Weaker1900to1950	As no. 5, but weaker ERFari and ERFaci between 1900 and 1950 multiplying the AR6 forcings by a sine curve.	AR6	2019
9	Stronger1900to1950	As no. 5, but stronger ERFari and ERFaci between 1900 and 1950 multiplying the AR6 forcings by a sine curve.	AR6	2019
10	Weaker1950to1980	As no. 5, but weaker ERFari and ERFaci between 1950 and 1980 multiplying the AR6 forcings by a sine curve.	AR6	2019
11	Stronger1950to1980	As no. 5, but stronger ERFari and ERFaci between 1950 and 1980 multiplying the AR6 forcings by a sine curve.	AR6	2019
12	StrongerWeaker1980to2019	As no. 5, but stronger and then weaker ERFari and ERFaci between 1980 and 2019 multiplying the AR6 forcings by a sine curve.	AR6	2019
13	Stronger1980to2019	As no. 5, but stronger ERFari and ERFaci between 1980 and 2019 multiplying the AR6 forcings by a sine curve.	AR6	2019
14	LinWeaker2014to2019	As no. 5, but linearly weaker ERFari and ERFaci from 2014 to 2019. The ERFari and ERFaci is weaker in 2019 than in AR6.	AR6	2019
15	Linear1950to1990	As no. 6, but with a linear ERFari and ERFaci between 1950 and 1990.	AR6	2019
16	Linear1950to2000	As no. 6, but with a linear ERFari and ERFaci between 1950 and 2000.	AR6	2019
17	Linear1950to2010	As no. 6, but with a linear ERFari and ERFaci between 1950 and 2010.	AR6	2019
18	Linear1950to2019	As no. 6, but with a linear ERFari and ERFaci between 1950 and 2019.	AR6	2019
19	Linear1950to1980 then flat	As no. 6, but with a linear ERFari and ERFaci between 1950 and 1980 and constant ERFari and ERFaci thereafter.	AR6	2019
20	Linear1950to1990 then flat	As no. 6, but with a linear ERFari and ERFaci between 1950 and 1990 and constant ERFari and ERFaci thereafter.	AR6	2019
21	Linear1950to2000 then flat	As no. 6, but with a linear ERFari and ERFaci between 1950 and 2000 and constant ERFari and ERFaci thereafter.	AR6	2019
	Extension up to 2022			
22	Replace AR6 prior with AR6 extended	Same as no. 5 but replace the AR6 prior ERF priors with the extended AR6 ERF time series (Forster et al., 2023).	AR6 extended	2019
23	Updata obs. end year 2019	Same as no. 22 but update all observational-based time series.	AR6 extended	2019
24	Base extended (end year 2022)	Same as no. 23 but extend from 2019 to 2022.	AR6 extended	2022
	ERFaci trend test			
25	Unc. in 1950 and 2010 independent	Same as no. 24 but uncertainties in 1950 (and before) and 2014 (and after) independent of each other; uncertainty scaling factor linearly interpolated for the years in between.	AR6 extended	2022

Code availability. The code to reproduce the figures in this paper can be found at https://doi.org/10.5281/zenodo.13837268 (Skeie, 2024).

Data availability. The data needed to reproduce the figures in the paper can be found at https://doi.org/10.5281/zenodo.13837268 (Skeie, 2024). Observational data used are presented and available via links provided in Table A2. ERF time series are available for AR6 at https://doi.org/10.5281/zenodo.5211357 (C. J. Smith et al., 2021) and for AR6 extended at https://github.com/ClimateIndicator/forcing-timeseries/releases/tag/v6.1.0 (Smith and Forster, 2022).

Supplement. The supplement related to this article is available online at: https://doi.org/10.5194/esd-15-1435-2024-supplement.

Author contributions. RBS wrote the paper and made the figures. RBS prepared the data and designed the experiments. MH and RBH performed the Bayesian estimation. All co-authors discussed the design and results and contributed to the writing.

Competing interests. The contact author has declared that none of the authors has any competing interests.

Disclaimer. Publisher's note: Copernicus Publications remains neutral with regard to jurisdictional claims made in the text, published maps, institutional affiliations, or any other geographical representation in this paper. While Copernicus Publications makes every effort to include appropriate place names, the final responsibility lies with the authors.

Acknowledgements. The work was funded through the Norwegian Research Council (grant no. 314997) and by the European Union's Horizon 2020 research and innovation program under grant agreement no. 821205 (FORCeS). We kindly acknowledge all the observational data providers listed in Table A2.

Financial support. This research has been supported by the Norges Forskningsråd (grant no. 314997) and Horizon 2020 (grant no. 821205).

Review statement. This paper was edited by Martin Wild and reviewed by two anonymous referees.

References

Aas, W., Mortier, A., Bowersox, V., Cherian, R., Faluvegi, G., Fagerli, H., Hand, J., Klimont, Z., Galy-Lacaux, C., Lehmann, C. M. B., Myhre, C. L., Myhre, G., Olivié, D., Sato, K., Quaas, J., Rao, P. S. P., Schulz, M., Shindell, D., Skeie, R. B., Stein, A., Takemura, T., Tsyro, S., Vet, R., and Xu, X.: Global and regional trends of atmospheric sulfur, Sci. Rep.-UK, 9, 953, https://doi.org/10.1038/s41598-018-37304-0, 2019.

Albright, A. L., Proistosescu, C., and Huybers, P.: Origins of a Relatively Tight Lower Bound on Anthropogenic Aerosol Radiative Forcing from Bayesian Analysis of Historical Observations, J. Climate, 34, 8777–8792, https://doi.org/10.1175/JCLI-D-21-0167.1, 2021.

Aldrin, M., Holden, M., Guttorp, P., Skeie, R. B., Myhre, G., and Berntsen, T. K.: Bayesian estimation of climate sensitivity based on a simple climate model fitted to observations of hemispheric temperatures and global ocean heat content, Environmetrics, 23, 253–271, https://doi.org/10.1002/env.2140, 2012.

Andrews, T., Gregory, J. M., and Webb, M. J.: The Dependence of Radiative Forcing and Feedback on Evolving Patterns of Surface Temperature Change in Climate Models, J. Climate, 28, 1630–1648, https://doi.org/10.1175/JCLI-D-14-00545.1, 2015.

Andrews, T., Gregory, J. M., Paynter, D., Silvers, L. G., Zhou, C., Mauritsen, T., Webb, M. J., Armour, K. C., Forster, P. M., and Titchner, H.: Accounting for Changing Temperature Patterns Increases Historical Estimates of Climate Sensitivity, Geophys. Res. Lett., 45, 8490–8499, https://doi.org/10.1029/2018GL078887, 2018.

Andrews, T., Bodas-Salcedo, A., Gregory, J. M., Dong, Y., Armour, K. C., Paynter, D., Lin, P., Modak, A., Mauritsen, T., Cole, J. N. S., Medeiros, B., Benedict, J. J., Douville, H., Roehrig, R., Koshiro, T., Kawai, H., Ogura, T., Dufresne, J.-L., Allan, R. P., and Liu, C.: On the Effect of Historical SST Patterns on Radiative Feedback, J. Geophys. Res., 127, e2022JD036675, https://doi.org/10.1029/2022JD036675, 2022.

Armour, K. C.: Energy budget constraints on climate sensitivity in light of inconstant climate feedbacks, Nat. Clim. Change, 7, 331–335, https://doi.org/10.1038/nclimate3278, 2017.

Armour, K. C., Proistosescu, C., Dong, Y., Hahn, L. C., Blanchard-Wrigglesworth, E., Pauling, A. G., Jnglin Wills, R. C., Andrews, T., Stuecker, M. F., Po-Chedley, S., Mitevski, I., Forster, P. M., and Gregory, J. M.: Sea-surface temperature pattern effects have slowed global warming and biased warming-based constraints on climate sensitivity, P. Natl. Acad. Sci. USA, 121, e2312093121, https://doi.org/10.1073/pnas.2312093121, 2024.

Bellouin, N., Quaas, J., Gryspeerdt, E., Kinne, S., Stier, P., Watson-Parris, D., Boucher, O., Carslaw, K. S., Christensen, M., Daniau, A. L., Dufresne, J. L., Feingold, G., Fiedler, S., Forster, P., Gettelman, A., Haywood, J. M., Lohmann, U., Malavelle, F., Mauritsen, T., McCoy, D. T., Myhre, G., Mülmenstädt, J., Neubauer, D., Possner, A., Rugenstein, M., Sato, Y., Schulz, M., Schwartz, S. E., Sourdeval, O., Storelvmo, T., Toll, V., Winker, D., and Stevens, B.: Bounding Global Aerosol Radiative Forcing of Climate Change, Rev. Geophys., 58, e2019RG000660, https://doi.org/10.1029/2019RG000660, 2020.

Bloch-Johnson, J., Rugenstein, M., Stolpe, M. B., Rohrschneider, T., Zheng, Y., and Gregory, J. M.: Climate Sensitivity Increases Under Higher CO_2 Levels Due to Feedback Temperature Dependence, Geophys. Res. Lett., 48, e2020GL089074, https://doi.org/10.1029/2020GL089074, 2021.

Bond, T. C., Bhardwaj, E., Dong, R., Jogani, R., Jung, S. K., Roden, C., Streets, D. G., and Trautmann, N. M.: Historical emissions of black and organic carbon aerosol from energy-related

combustion, 1850–2000, Global Biogeochem. Cy., 21, Gb2018, https://doi.org/10.1029/2006gb002840, 2007.

Cess, R. D., Zhang, M.-H., Potter, G. L., Barker, H. W., Colman, R. A., Dazlich, D. A., Del Genio, A. D., Esch, M., Fraser, J. R., Galin, V., Gates, W. L., Hack, J. J., Ingram, W. J., Kiehl, J. T., Lacis, A. A., Le Treut, H., Li, Z.-X., Liang, X.-Z., Mahfouf, J.-F., McAvaney, B. J., Meleshko, V. P., Morcrette, J.-J., Randall, D. A., Roeckner, E., Royer, J.-F., Sokolov, A. P., Sporyshev, P. V., Taylor, K. E., Wang, W.-C., and Wetherald, R. T.: Uncertainties in Carbon Dioxide Radiative Forcing in Atmospheric General Circulation Models, Science, 262, 1252–1255, https://doi.org/10.1126/science.262.5137.1252, 1993.

Cheng, L., Zhu, J., Cowley, R., Boyer, T., and Wijffels, S.: Time, Probe Type, and Temperature Variable Bias Corrections to Historical Expendable Bathythermograph Observations, J. Atmos. Ocean. Tech., 31, 1793–1825, https://doi.org/10.1175/JTECH-D-13-00197.1, 2014.

Cheng, L., Trenberth, K. E., Fasullo, J., Boyer, T., Abraham, J., and Zhu, J.: Improved estimates of ocean heat content from 1960 to 2015, Sci. Adv., 3, e1601545, https://doi.org/10.1126/sciadv.1601545, 2017.

Cheng, L., Abraham, J., Hausfather, Z., and Trenberth, K. E.: How fast are the oceans warming?, Science, 363, 128, https://doi.org/10.1126/science.aav7619, 2019a.

Cheng, L., Trenberth, K. E., Fasullo, J. T., Mayer, M., Balmaseda, M., and Zhu, J.: Evolution of Ocean Heat Content Related to ENSO, J. Climate, 32, 3529–3556, https://doi.org/10.1175/JCLI-D-18-0607.1, 2019b.

Cheng, L., Abraham, J., Zhu, J., Trenberth, K. E., Fasullo, J., Boyer, T., Locarnini, R., Zhang, B., Yu, F., Wan, L., Chen, X., Song, X., Liu, Y., and Mann, M. E.: Record-Setting Ocean Warmth Continued in 2019, Adv. Atmos. Sci., 37, 137–142, https://doi.org/10.1007/s00376-020-9283-7, 2020.

Cheng, L., Abraham, J., Trenberth, K. E., Fasullo, J., Boyer, T., Mann, M. E., Zhu, J., Wang, F., Locarnini, R., Li, Y., Zhang, B., Tan, Z., Yu, F., Wan, L., Chen, X., Song, X., Liu, Y., Reseghetti, F., Simoncelli, S., Gouretski, V., Chen, G., Mishonov, A., and Reagan, J.: Another Record: Ocean Warming Continues through 2021 despite La Niña Conditions, Adv. Atmos. Sci., 39, 373–385, https://doi.org/10.1007/s00376-022-1461-3, 2022.

Collins, W. J., Lamarque, J.-F., Schulz, M., Boucher, O., Eyring, V., Hegglin, M. I., Maycock, A., Myhre, G., Prather, M., Shindell, D., and Smith, S. J.: AerChemMIP: quantifying the effects of chemistry and aerosols in CMIP6, Geosci. Model Dev., 10, 585–607, https://doi.org/10.5194/gmd-10-585-2017, 2017.

Dessler, A. E.: Potential Problems Measuring Climate Sensitivity from the Historical Record, J. Climate, 33, 2237–2248, https://doi.org/10.1175/JCLI-D-19-0476.1, 2020.

Domingues, C. M., Church, J. A., White, N. J., Gleckler, P. J., Wijffels, S. E., Barker, P. M., and Dunn, J. R.: Improved estimates of upper-ocean warming and multi-decadal sea-level rise, Nature, 453, 1090–1093, https://doi.org/10.1038/nature07080, 2008.

Flynn, C. M. and Mauritsen, T.: On the climate sensitivity and historical warming evolution in recent coupled model ensembles, Atmos. Chem. Phys., 20, 7829–7842, https://doi.org/10.5194/acp-20-7829-2020, 2020.

Flynn, C. M., Huusko, L., Modak, A., and Mauritsen, T.: Strong aerosol cooling alone does not explain cold-biased mid-century temperatures in CMIP6 models, Atmos. Chem. Phys., 23, 15121–15133, https://doi.org/10.5194/acp-23-15121-2023, 2023.

Forster, P., Storelvmo, T., Armour, K., Collins, W., Dufresne, J. L., Frame, D., Lunt, D. J., Mauritsen, T., Palmer, M. D., Watanabe, M., Wild, M., and Zhang, H.: The Earth's Energy Budget, Climate Feedbacks, and Climate Sensitivity, in: Climate Change 2021: The Physical Science Basis. Contribution of Working Group I to the Sixth Assessment Report of the Intergovernmental Panel on Climate Change, edited by: Masson-Delmotte, V., Zhai, P., Pirani, A., Connors, S. L., Péan, C., Berger, S., Caud, N., Chen, Y., Goldfarb, L., Gomis, M. I., Huang, M., Leitzell, K., Lonnoy, E., Matthews, J. B. R., Maycock, T. K., Waterfield, T., Yelekçi, O., Yu, R., and Zhou, B., Cambridge University Press, Cambridge, United Kingdom and New York, NY, USA, https://doi.org/10.1017/9781009157896.009, 2021.

Forster, P. M.: Inference of Climate Sensitivity from Analysis of Earth's Energy Budget, Annu. Rev. Earth Pl. Sc., 44, 85–106, https://doi.org/10.1146/annurev-earth-060614-105156, 2016.

Forster, P. M., Smith, C. J., Walsh, T., Lamb, W. F., Lamboll, R., Hauser, M., Ribes, A., Rosen, D., Gillett, N., Palmer, M. D., Rogelj, J., von Schuckmann, K., Seneviratne, S. I., Trewin, B., Zhang, X., Allen, M., Andrew, R., Birt, A., Borger, A., Boyer, T., Broersma, J. A., Cheng, L., Dentener, F., Friedlingstein, P., Gutiérrez, J. M., Gütschow, J., Hall, B., Ishii, M., Jenkins, S., Lan, X., Lee, J.-Y., Morice, C., Kadow, C., Kennedy, J., Killick, R., Minx, J. C., Naik, V., Peters, G. P., Pirani, A., Pongratz, J., Schleussner, C.-F., Szopa, S., Thorne, P., Rohde, R., Rojas Corradi, M., Schumacher, D., Vose, R., Zickfeld, K., Masson-Delmotte, V., and Zhai, P.: Indicators of Global Climate Change 2022: annual update of large-scale indicators of the state of the climate system and human influence, Earth Syst. Sci. Data, 15, 2295–2327, https://doi.org/10.5194/essd-15-2295-2023, 2023.

Forster, P. M., Smith, C., Walsh, T., Lamb, W. F., Lamboll, R., Hall, B., Hauser, M., Ribes, A., Rosen, D., Gillett, N. P., Palmer, M. D., Rogelj, J., von Schuckmann, K., Trewin, B., Allen, M., Andrew, R., Betts, R. A., Borger, A., Boyer, T., Broersma, J. A., Buontempo, C., Burgess, S., Cagnazzo, C., Cheng, L., Friedlingstein, P., Gettelman, A., Gütschow, J., Ishii, M., Jenkins, S., Lan, X., Morice, C., Mühle, J., Kadow, C., Kennedy, J., Killick, R. E., Krummel, P. B., Minx, J. C., Myhre, G., Naik, V., Peters, G. P., Pirani, A., Pongratz, J., Schleussner, C.-F., Seneviratne, S. I., Szopa, S., Thorne, P., Kovilakam, M. V. M., Majamäki, E., Jalkanen, J.-P., van Marle, M., Hoesly, R. M., Rohde, R., Schumacher, D., van der Werf, G., Vose, R., Zickfeld, K., Zhang, X., Masson-Delmotte, V., and Zhai, P.: Indicators of Global Climate Change 2023: annual update of key indicators of the state of the climate system and human influence, Earth Syst. Sci. Data, 16, 2625–2658, https://doi.org/10.5194/essd-16-2625-2024, 2024.

Fueglistaler, S. and Silvers, L. G.: The Peculiar Trajectory of Global Warming, J. Geophys. Res., 126, e2020JD033629, https://doi.org/10.1029/2020JD033629, 2021.

Gillett, N. P., Kirchmeier-Young, M., Ribes, A., Shiogama, H., Hegerl, G. C., Knutti, R., Gastineau, G., John, J. G., Li, L., Nazarenko, L., Rosenbloom, N., Seland, Ø., Wu, T., Yukimoto, S., and Ziehn, T.: Constraining human contributions to observed warming since the pre-industrial period, Nat. Clim. Change, 11, 207–212, https://doi.org/10.1038/s41558-020-00965-9, 2021.

GISTEMP-Team: GISS Surface Temperature Analysis (GISTEMP), version 4, NASA Goddard Institute for Space Studies, https://data.giss.nasa.gov/gistemp/, last access: 23 June 2023.

Good, S. A., Martin, M. J., and Rayner, N. A.: EN4: Quality controlled ocean temperature and salinity profiles and monthly objective analyses with uncertainty estimates, J. Geophys. Res.-Oceans, 118, 6704–6716, https://doi.org/10.1002/2013JC009067, 2013.

Gouretski, V. and Cheng, L.: Correction for Systematic Errors in the Global Dataset of Temperature Profiles from Mechanical Bathythermographs, J. Atmos. Ocean. Tech., 37, 841–855, https://doi.org/10.1175/JTECH-D-19-0205.1, 2020.

Gregory, J. M., Ingram, W. J., Palmer, M. A., Jones, G. S., Stott, P. A., Thorpe, R. B., Lowe, J. A., Johns, T. C., and Williams, K. D.: A new method for diagnosing radiative forcing and climate sensitivity, Geophys. Res. Lett., 31, L03205, https://doi.org/10.1029/2003gl018747, 2004.

Gregory, J. M., Andrews, T., Ceppi, P., Mauritsen, T., and Webb, M. J.: How accurately can the climate sensitivity to CO_2 be estimated from historical climate change?, Clim. Dynam., 54, 129–157, https://doi.org/10.1007/s00382-019-04991-y, 2020.

Gulev, S. K., Thorne, P. W., Ahn, J., Dentener, F. J., Domingues, C. M., Gerland, S., Gong, D., Kaufman, D. S., Nnamchi, H. C., Quaas, J., Rivera, J. A., Sathyendranath, S., Smith, S. L., Trewin, B., von Shuckmann, K., and Vose, R. S.: Changing State of the Climate System, in: Climate Change 2021: The Physical Science Basis. Contribution of Working Group I to the Sixth Assessment Report of the Intergovernmental Panel on Climate Change, edited by: Masson-Delmotte, V., Zhai, P., Pirani, A., Connors, S. L., Péan, C., Berger, S., Caud, N., Chen, Y., Goldfarb, L., Gomis, M. I., Huang, M., Leitzell, K., Lonnoy, E., Matthews, J. B. R., Maycock, T. K., Waterfield, T., Yelekçi, O., Yu, R., and Zhou, B., Cambridge University Press, https://doi.org/10.1017/9781009157896.004, 2021a.

Gulev, S. K., Thorne, P. W., Ahn, J., Dentener, F. J., Domingues, C. M., Gerland, S., Gong, D., Kaufman, D. S., Nnamchi, H. C., Quaas, J., Rivera, J. A., Sathyendranath, S., Smith, S. L., Trewin, B., von Shuckmann, K., and Vose, R. S.: Changing State of the Climate System Supplementary Material, in: Climate Change 2021: The Physical Science Basis. Contribution of Working Group I to the Sixth Assessment Report of the Intergovernmental Panel on Climate Change, edited by: Masson-Delmotte, V., Zhai, P., Pirani, A., Connors, S. L., Péan, C., Berger, S., Caud, N., Chen, Y., Goldfarb, L., Gomis, M. I., Huang, M., Leitzell, K., Lonnoy, E., Matthews, J. B. R., Maycock, T. K., Waterfield, T., Yelekçi, O., Yu, R., and Zhou, B., 2021b.

Hansen, J., Nazarenko, L., Ruedy, R., Sato, M., Willis, J., Genio, A. D., Koch, D., Lacis, A., Lo, K., Menon, S., Novakov, T., Perlwitz, J., Russell, G., Schmidt, G. A., and Tausnev, N.: Earth's Energy Imbalance: Confirmation and Implications, Science, 308, 1431–1435, https://doi.org/10.1126/science.1110252, 2005.

Hawkins, E. and Sutton, R.: The Potential to Narrow Uncertainty in Regional Climate Predictions, B. Am. Meteorol. Soc., 90, 1095–1107, https://doi.org/10.1175/2009bams2607.1, 2009.

He, H., Kramer, R. J., Soden, B. J., and Jeevanjee, N.: State dependence of CO_2 forcing and its implications for climate sensitivity, Science, 382, 1051–1056, https://doi.org/10.1126/science.abq6872, 2023.

Hodnebrog, Ø., Myhre, G., Jouan, C., Andrews, T., Forster, P. M., Jia, H., Loeb, N. G., Olivié, D. J. L., Paynter, D., Quaas, J., Raghuraman, S. P., and Schulz, M.: Recent reductions in aerosol emissions have increased Earth's energy imbalance, Communications Earth & Environment, 5, 166, https://doi.org/10.1038/s43247-024-01324-8, 2024.

Hoesly, R. M., Smith, S. J., Feng, L., Klimont, Z., Janssens-Maenhout, G., Pitkanen, T., Seibert, J. J., Vu, L., Andres, R. J., Bolt, R. M., Bond, T. C., Dawidowski, L., Kholod, N., Kurokawa, J.-I., Li, M., Liu, L., Lu, Z., Moura, M. C. P., O'Rourke, P. R., and Zhang, Q.: Historical (1750–2014) anthropogenic emissions of reactive gases and aerosols from the Community Emissions Data System (CEDS), Geosci. Model Dev., 11, 369–408, https://doi.org/10.5194/gmd-11-369-2018, 2018.

Hwang, Y.-T., Xie, S.-P., Chen, P.-J., Tseng, H.-Y., and Deser, C.: Contribution of anthropogenic aerosols to persistent La Niña-like conditions in the early 21st century, P. Natl. Acad. Sci. USA, 121, e2315124121, https://doi.org/10.1073/pnas.2315124121, 2024.

Ishii, M., Fukuda, Y., Hirahara, S., Yasui, S., Suzuki, T., and Sato, K.: Accuracy of Global Upper Ocean Heat Content Estimation Expected from Present Observational Data Sets, SOLA, 13, 163–167, https://doi.org/10.2151/sola.2017-030, 2017.

Johansson, D. J. A., O'Neill, B. C., Tebaldi, C., and Haggstrom, O.: Equilibrium climate sensitivity in light of observations over the warming hiatus, Nat. Clim. Change, 5, 449–453, https://doi.org/10.1038/nclimate2573, 2015.

Kasoar, M., Shawki, D., and Voulgarakis, A.: Similar spatial patterns of global climate response to aerosols from different regions, npj Climate and Atmospheric Science, 1, 12, https://doi.org/10.1038/s41612-018-0022-z, 2018.

Knutti, R., Rugenstein, M. A. A., and Hegerl, G. C.: Beyond equilibrium climate sensitivity, Nat. Geosci., 10, 727, https://doi.org/10.1038/ngeo3017, 2017.

Lenssen, N. J. L., Schmidt, G. A., Hansen, J. E., Menne, M. J., Persin, A., Ruedy, R., and Zyss, D.: Improvements in the GISTEMP Uncertainty Model, J. Geophys. Res., 124, 6307–6326, https://doi.org/10.1029/2018JD029522, 2019.

Levitus, S., Antonov, J. I., Boyer, T. P., Baranova, O. K., Garcia, H. E., Locarnini, R. A., Mishonov, A. V., Reagan, J. R., Seidov, D., Yarosh, E. S., and Zweng, M. M.: World ocean heat content and thermosteric sea level change (0–2000 m), 1955–2010, Geophys. Res. Lett., 39, L10603, https://doi.org/10.1029/2012GL051106, 2012.

Li, Z., England, M. H., and Groeskamp, S.: Recent acceleration in global ocean heat accumulation by mode and intermediate waters, Nat. Commun., 14, 6888, https://doi.org/10.1038/s41467-023-42468-z, 2023.

Loeb, N. G., Doelling, D. R., Wang, H., Su, W., Nguyen, C., Corbett, J. G., Liang, L., Mitrescu, C., Rose, F. G., and Kato, S.: Clouds and the Earth's Radiant Energy System (CERES) Energy Balanced and Filled (EBAF) Top-of-Atmosphere (TOA) Edition-4.0 Data Product, J. Climate, 31, 895–918, https://doi.org/10.1175/JCLI-D-17-0208.1, 2018a.

Loeb, N. G., Thorsen, T. J., Norris, J. R., Wang, H., and Su, W.: Changes in Earth's Energy Budget during and after the "Pause" in Global Warming: An Observational Perspective, Climate, 6, https://doi.org/10.3390/cli6030062, 2018b.

Loeb, N. G., Johnson, G. C., Thorsen, T. J., Lyman, J. M., Rose, F. G., and Kato, S.: Satellite and Ocean Data Reveal Marked

Increase in Earth's Heating Rate, Geophys. Res. Lett., 48, e2021GL093047, https://doi.org/10.1029/2021GL093047, 2021.

Lund, M. T., Myhre, G., Skeie, R. B., Samset, B. H., and Klimont, Z.: Implications of differences between recent anthropogenic aerosol emission inventories for diagnosed AOD and radiative forcing from 1990 to 2019, Atmos. Chem. Phys., 23, 6647–6662, https://doi.org/10.5194/acp-23-6647-2023, 2023.

Lyman, J. M. and Johnson, G. C.: Estimating Global Ocean Heat Content Changes in the Upper 1800 m since 1950 and the Influence of Climatology Choice, J. Climate, 27, 1945–1957, https://doi.org/10.1175/jcli-d-12-00752.1, 2014.

Manktelow, P. T., Mann, G. W., Carslaw, K. S., Spracklen, D. V., and Chipperfield, M. P.: Regional and global trends in sulfate aerosol since the 1980s, Geophys. Res. Lett., 34, L14803, https://doi.org/10.1029/2006GL028668, 2007.

Minière, A., von Schuckmann, K., Sallée, J.-B., and Vogt, L.: Robust acceleration of Earth system heating observed over the past six decades, Sci. Rep.-UK, 13, 22975, https://doi.org/10.1038/s41598-023-49353-1, 2023.

Morice, C. P., Kennedy, J. J., Rayner, N. A., Winn, J. P., Hogan, E., Killick, R. E., Dunn, R. J. H., Osborn, T. J., Jones, P. D., and Simpson, I. R.: An Updated Assessment of Near-Surface Temperature Change From 1850: The HadCRUT5 Data Set, J. Geophys. Res., 126, e2019JD032361, https://doi.org/10.1029/2019JD032361, 2021.

Myhre, G., Samset, B. H., Schulz, M., Balkanski, Y., Bauer, S., Berntsen, T. K., Bian, H., Bellouin, N., Chin, M., Diehl, T., Easter, R. C., Feichter, J., Ghan, S. J., Hauglustaine, D., Iversen, T., Kinne, S., Kirkevåg, A., Lamarque, J.-F., Lin, G., Liu, X., Lund, M. T., Luo, G., Ma, X., van Noije, T., Penner, J. E., Rasch, P. J., Ruiz, A., Seland, Ø., Skeie, R. B., Stier, P., Takemura, T., Tsigaridis, K., Wang, P., Wang, Z., Xu, L., Yu, H., Yu, F., Yoon, J.-H., Zhang, K., Zhang, H., and Zhou, C.: Radiative forcing of the direct aerosol effect from AeroCom Phase II simulations, Atmos. Chem. Phys., 13, 1853–1877, https://doi.org/10.5194/acp-13-1853-2013, 2013a.

Myhre, G., Shindell, D., Bréon, F.-M., Collins, W., Fuglestvedt, J., Huang, J., Koch, D., Lamarque, J.-F., Lee, D., Mendoza, B., Nakajima, T., Robock, A., Stephens, G., Takemura, T., and Zhang, H.: Anthropogenic and Natural Radiative Forcing, in: Climate Change 2013: The Physical Science Basis. Contribution of Working Group I to the Fifth Assessment Report of the Intergovernmental Panel on Climate Change edited by: Stocker, T. F., Qin, D., Plattner, G.-K., Tignor, M., Allen, S. K., Boschung, J., Nauels, A., Xia, Y., Bex, V., and Midgley, P. M., Cambridge University Press, Cambridge, United Kingdom and New York, NY, USA, ISBN 978-1-107-05799-1, 2013b.

Pincus, R., Forster, P. M., and Stevens, B.: The Radiative Forcing Model Intercomparison Project (RFMIP): experimental protocol for CMIP6, Geosci. Model Dev., 9, 3447–3460, https://doi.org/10.5194/gmd-9-3447-2016, 2016.

Quaas, J., Jia, H., Smith, C., Albright, A. L., Aas, W., Bellouin, N., Boucher, O., Doutriaux-Boucher, M., Forster, P. M., Grosvenor, D., Jenkins, S., Klimont, Z., Loeb, N. G., Ma, X., Naik, V., Paulot, F., Stier, P., Wild, M., Myhre, G., and Schulz, M.: Robust evidence for reversal of the trend in aerosol effective climate forcing, Atmos. Chem. Phys., 22, 12221–12239, https://doi.org/10.5194/acp-22-12221-2022, 2022.

Raghuraman, S. P., Paynter, D., and Ramaswamy, V.: Anthropogenic forcing and response yield observed positive trend in Earth's energy imbalance, Nat. Commun., 12, 4577, https://doi.org/10.1038/s41467-021-24544-4, 2021.

Raghuraman, S. P., Paynter, D., Menzel, R., and Ramaswamy, V.: Forcing, Cloud Feedbacks, Cloud Masking, and Internal Variability in the Cloud Radiative Effect Satellite Record, J. Climate, 36, 4151–4167, https://doi.org/10.1175/JCLI-D-22-0555.1, 2023.

Rugenstein, M., Bloch-Johnson, J., Gregory, J., Andrews, T., Mauritsen, T., Li, C., Frölicher, T. L., Paynter, D., Danabasoglu, G., Yang, S., Dufresne, J.-L., Cao, L., Schmidt, G. A., Abe-Ouchi, A., Geoffroy, O., and Knutti, R.: Equilibrium Climate Sensitivity Estimated by Equilibrating Climate Models, Geophys. Res. Lett., 47, e2019GL083898, https://doi.org/10.1029/2019GL083898, 2020.

Samset, B. H., Myhre, G., Herber, A., Kondo, Y., Li, S.-M., Moteki, N., Koike, M., Oshima, N., Schwarz, J. P., Balkanski, Y., Bauer, S. E., Bellouin, N., Berntsen, T. K., Bian, H., Chin, M., Diehl, T., Easter, R. C., Ghan, S. J., Iversen, T., Kirkevåg, A., Lamarque, J.-F., Lin, G., Liu, X., Penner, J. E., Schulz, M., Seland, Ø., Skeie, R. B., Stier, P., Takemura, T., Tsigaridis, K., and Zhang, K.: Modelled black carbon radiative forcing and atmospheric lifetime in AeroCom Phase II constrained by aircraft observations, Atmos. Chem. Phys., 14, 12465–12477, https://doi.org/10.5194/acp-14-12465-2014, 2014.

Sandstad, M., Aamaas, B., Johansen, A. N., Lund, M. T., Peters, G. P., Samset, B. H., Sanderson, B. M., and Skeie, R. B.: CICERO Simple Climate Model (CICERO-SCM v1.1.1) – an improved simple climate model with a parameter calibration tool, Geosci. Model Dev., 17, 6589–6625, https://doi.org/10.5194/gmd-17-6589-2024, 2024.

Schlesinger, M. E. and Jiang, X. J.: Simple-model representation of atmosphere-ocean GCMs and estimation of the time scale of CO_2-induced climate change, J. Climate, 3, 1297–1315, 1990.

Schlesinger, M. E., Jiang, X., and Charlson, R. J.: Implication of Anthropogenic Atmospheric Sulphate for the Sensitivity of the Climate System, in: Climate Change and Energy Policy: Proceedings of the International Conference on Global Climate Change: Its Mitigation Through Improved Production and Use of Energy, edited by: Rosen, L. and Glasser, R., American Institute of Physics, New York, 75–108, 1992.

Senior, C. A. and Mitchell, J. F. B.: The time-dependence of climate sensitivity, Geophys. Res. Lett., 27, 2685–2688, 2000.

Sherwood, S., Webb, M. J., Annan, J. D., Armour, K. C., Forster, P. M., Hargreaves, J. C., Hegerl, G., Klein, S. A., Marvel, K. D., Rohling, E. J., Watanabe, M., Andrews, T., Braconnot, P., Bretherton, C. S., Foster, G. L., Hausfather, Z., von der Heydt, A. S., Knutti, R., Mauritsen, T., Norris, J. R., Proistosescu, C., Rugenstein, M., Schmidt, G. A., Tokarska, K. B., and Zelinka, M. D.: An assessment of Earth's climate sensitivity using multiple lines of evidence, Rev. Geophys., 58, e2019RG000678, https://doi.org/10.1029/2019RG000678, 2020.

Sherwood, S. C., Bony, S., Boucher, O., Bretherton, C., Forster, P. M., Gregory, J. M., and Stevens, B.: Adjustments in the Forcing-Feedback Framework for Understanding Climate Change, B. Am. Meteorol. Soc., 96, 217–228, https://doi.org/10.1175/BAMS-D-13-00167.1, 2015.

Shindell, D. T., Faluvegi, G., Rotstayn, L., and Milly, G.: Spatial patterns of radiative forcing and surface temperature response, J. Geophys. Res., 120, 5385–5403, https://doi.org/10.1002/2014JD022752, 2015.

Skeie, R. B.: ragnhibs/climsens_24: v1.0, Zenodo [code, data set], https://doi.org/10.5281/zenodo.13837268, 2024.

Skeie, R. B., Berntsen, T., Aldrin, M., Holden, M., and Myhre, G.: A lower and more constrained estimate of climate sensitivity using updated observations and detailed radiative forcing time series, Earth Syst. Dynam., 5, 139–175, https://doi.org/10.5194/esd-5-139-2014, 2014.

Skeie, R. B., Berntsen, T., Aldrin, M., Holden, M., and Myhre, G.: Climate sensitivity estimates – sensitivity to radiative forcing time series and observational data, Earth Syst. Dynam., 9, 879–894, https://doi.org/10.5194/esd-9-879-2018, 2018.

Skeie, R. B., Myhre, G., Hodnebrog, Ø., Cameron-Smith, P. J., Deushi, M., Hegglin, M. I., Horowitz, L. W., Kramer, R. J., Michou, M., Mills, M. J., Olivié, D. J. L., Connor, F. M. O., Paynter, D., Samset, B. H., Sellar, A., Shindell, D., Takemura, T., Tilmes, S., and Wu, T.: Historical total ozone radiative forcing derived from CMIP6 simulations, npj Climate and Atmospheric Science, 3, 32, https://doi.org/10.1038/s41612-020-00131-0, 2020.

Smith, C. and Forster, P.: IPCC AR6 WG1 forcing updated to 2022, https://github.com/ClimateIndicator/forcing-timeseries/releases/tag/v6.1.0 (last access: 1 July 2024), 2022.

Smith, C., Nicholls, Z. R. J., Armour, K., Collins, W., Forster, P. Meinshausen, M., Palmer, M. D., and Watanabe, M.: The Earth's Energy Budget, Climate Feedbacks, and Climate Sensitivity Supplementary Material, in: Climate Change 2021: The Physical Science Basis. Contribution of Working Group I to the Sixth Assessment Report of the Intergovernmental Panel on Climate Change, edited by: Masson-Delmotte, V., Zhai, P., Pirani, A., Connors, S. L., Péan, C., Berger, S., Caud, N., Chen, Y., Goldfarb, L., Gomis, M. I., Huang, M., Leitzell, K., Lonnoy, E., Matthews, J. B. R., Maycock, T. K., Waterfield, T., Yelekçi, O., Yu, R., and Zhou, B., https://www.ipcc.ch/ (last access: 1 July 2024), 2021.

Smith, C. J. and Forster, P. M.: Suppressed Late-20th Century Warming in CMIP6 Models Explained by Forcing and Feedbacks, Geophys. Res. Lett., 48, e2021GL094948, https://doi.org/10.1029/2021GL094948, 2021.

Smith, C. J., Kramer, R. J., Myhre, G., Alterskjær, K., Collins, W., Sima, A., Boucher, O., Dufresne, J.-L., Nabat, P., Michou, M., Yukimoto, S., Cole, J., Paynter, D., Shiogama, H., O'Connor, F. M., Robertson, E., Wiltshire, A., Andrews, T., Hannay, C., Miller, R., Nazarenko, L., Kirkevåg, A., Olivié, D., Fiedler, S., Lewinschal, A., Mackallah, C., Dix, M., Pincus, R., and Forster, P. M.: Effective radiative forcing and adjustments in CMIP6 models, Atmos. Chem. Phys., 20, 9591–9618, https://doi.org/10.5194/acp-20-9591-2020, 2020.

Smith, C. J., Forster, P. M., Berger, S., Collins, W., Hall, B., Lunt, D., Palmer, M. D., Watanabe, M., Cain, M., Harris, G., Leach, N. J., Ringer, M., and Zelinka, M.: Figure and data generation for Chapter 7 of the IPCC's Sixth Assessment Report, Working Group 1 (plus assorted other contributions), Version 1.0, Zenodo [data set], https://doi.org/10.5281/zenodo.5211357, 2021.

Smith, C. J., Harris, G. R., Palmer, M. D., Bellouin, N., Collins, W., Myhre, G., Schulz, M., Golaz, J. C., Ringer, M., Storelvmo, T., and Forster, P. M.: Energy Budget Constraints on the Time History of Aerosol Forcing and Climate Sensitivity, J. Geophys. Res., 126, e2020JD033622, https://doi.org/10.1029/2020JD033622, 2021.

Smith, S. J., van Aardenne, J., Klimont, Z., Andres, R. J., Volke, A., and Delgado Arias, S.: Anthropogenic sulfur dioxide emissions: 1850–2005, Atmos. Chem. Phys., 11, 1101–1116, https://doi.org/10.5194/acp-11-1101-2011, 2011.

Soden, B. J., Collins, W. D., and Feldman, D. R.: Reducing uncertainties in climate models, Science, 361, 326–327, https://doi.org/10.1126/science.aau1864, 2018.

Stevens, B., Sherwood, S. C., Bony, S., and Webb, M. J.: Prospects for narrowing bounds on Earth's equilibrium climate sensitivity, Earths Future, 4, 512–522, https://doi.org/10.1002/2016EF000376, 2016.

Su, H., Zhang, H., Geng, X., Qin, T., Lu, W., and Yan, X.-H.: OPEN: A New Estimation of Global Ocean Heat Content for Upper 2000 Meters from Remote Sensing Data, Remote Sens., 12, 2294, https://doi.org/10.3390/rs12142294, 2020.

Textor, C., Schulz, M., Guibert, S., Kinne, S., Balkanski, Y., Bauer, S., Berntsen, T., Berglen, T., Boucher, O., Chin, M., Dentener, F., Diehl, T., Feichter, J., Fillmore, D., Ginoux, P., Gong, S., Grini, A., Hendricks, J., Horowitz, L., Huang, P., Isaksen, I. S. A., Iversen, T., Kloster, S., Koch, D., Kirkevåg, A., Kristjansson, J. E., Krol, M., Lauer, A., Lamarque, J. F., Liu, X., Montanaro, V., Myhre, G., Penner, J. E., Pitari, G., Reddy, M. S., Seland, Ø., Stier, P., Takemura, T., and Tie, X.: The effect of harmonized emissions on aerosol properties in global models – an AeroCom experiment, Atmos. Chem. Phys., 7, 4489–4501, https://doi.org/10.5194/acp-7-4489-2007, 2007.

Tokarska, K. B., Stolpe, M. B., Sippel, S., Fischer, E. M., Smith, C. J., Lehner, F., and Knutti, R.: Past warming trend constrains future warming in CMIP6 models, Science Advances, 6, eaaz9549, https://doi.org/10.1126/sciadv.aaz9549, 2020.

UNFCCC: Adoption of the Paris Agreement FCCC/CP/2015/L.9/Rev. 1, http://unfccc.int/resource/docs/2015/cop21/eng/l09r01.pdf (last access: 1 July 2024), 2015.

von Schuckmann, K., Minière, A., Gues, F., Cuesta-Valero, F. J., Kirchengast, G., Adusumilli, S., Straneo, F., Ablain, M., Allan, R. P., Barker, P. M., Beltrami, H., Blazquez, A., Boyer, T., Cheng, L., Church, J., Desbruyeres, D., Dolman, H., Domingues, C. M., García-García, A., Giglio, D., Gilson, J. E., Gorfer, M., Haimberger, L., Hakuba, M. Z., Hendricks, S., Hosoda, S., Johnson, G. C., Killick, R., King, B., Kolodziejczyk, N., Korosov, A., Krinner, G., Kuusela, M., Landerer, F. W., Langer, M., Lavergne, T., Lawrence, I., Li, Y., Lyman, J., Marti, F., Marzeion, B., Mayer, M., MacDougall, A. H., McDougall, T., Monselesan, D. P., Nitzbon, J., Otosaka, I., Peng, J., Purkey, S., Roemmich, D., Sato, K., Sato, K., Savita, A., Schweiger, A., Shepherd, A., Seneviratne, S. I., Simons, L., Slater, D. A., Slater, T., Steiner, A. K., Suga, T., Szekely, T., Thiery, W., Timmermans, M.-L., Vanderkelen, I., Wjiffels, S. E., Wu, T., and Zemp, M.: Heat stored in the Earth system 1960–2020: where does the energy go?, Earth Syst. Sci. Data, 15, 1675–1709, https://doi.org/10.5194/essd-15-1675-2023, 2023.

Voosen, P.: The hottest year was even hotter than expected, Science, 383, 134–134, https://doi.org/10.1126/science.ztj60l9, 2024.

Vose, R. S., Huang, B., Yin, X., Arndt, D., Easterling, D. R., Lawrimore, J. H., Menne, M. J., Sanchez-Lugo, A., and Zhang, H. M.: Implementing Full Spatial Coverage in NOAA's Global Tem-

perature Analysis, Geophys. Res. Lett., 48, e2020GL090873, https://doi.org/10.1029/2020GL090873, 2021.

Watson-Parris, D. and Smith, C. J.: Large uncertainty in future warming due to aerosol forcing, Nat. Clim. Change, 12, 1111–1113, https://doi.org/10.1038/s41558-022-01516-0, 2022.

Wills, R. C. J., Dong, Y., Proistosecu, C., Armour, K. C., and Battisti, D. S.: Systematic Climate Model Biases in the Large-Scale Patterns of Recent Sea-Surface Temperature and Sea-Level Pressure Change, Geophys. Res. Lett., 49, e2022GL100011, https://doi.org/10.1029/2022GL100011, 2022.

Zelinka, M. D., Myers, T. A., McCoy, D. T., Po-Chedley, S., Caldwell, P. M., Ceppi, P., Klein, S. A., and Taylor, K. E.: Causes of Higher Climate Sensitivity in CMIP6 Models, Geophys. Res. Lett., 47, e2019GL085782, https://doi.org/10.1029/2019GL085782, 2020.

Zhang, J., Furtado, K., Turnock, S. T., Mulcahy, J. P., Wilcox, L. J., Booth, B. B., Sexton, D., Wu, T., Zhang, F., and Liu, Q.: The role of anthropogenic aerosols in the anomalous cooling from 1960 to 1990 in the CMIP6 Earth system models, Atmos. Chem. Phys., 21, 18609–18627, https://doi.org/10.5194/acp-21-18609-2021, 2021.

Zheng, B., Tong, D., Li, M., Liu, F., Hong, C., Geng, G., Li, H., Li, X., Peng, L., Qi, J., Yan, L., Zhang, Y., Zhao, H., Zheng, Y., He, K., and Zhang, Q.: Trends in China's anthropogenic emissions since 2010 as the consequence of clean air actions, Atmos. Chem. Phys., 18, 14095–14111, https://doi.org/10.5194/acp-18-14095-2018, 2018.

Zhou, C., Zelinka, M. D., Dessler, A. E., and Wang, M.: Greater committed warming after accounting for the pattern effect, Nat. Clim. Change, 11, 132–136, https://doi.org/10.1038/s41558-020-00955-x, 2021.